Structures and migrations of interfaces between β precipitates and α' matrix in a Ti-2.6 wt% Mo alloy

Jin-Yu Zhang, Yang-Sheng Zhang, Frédéric Mompiou, Wen-Zheng Zhang

Structures and migrations of interfaces between β precipitates and α′ matrix in a Ti-2.6 wt% Mo alloy

Jin-Yu Zhang [a,b,*], Yang-Sheng Zhang [a,c], Frédéric Mompiou [c], Wen-Zheng Zhang [a,d,*]

[a] Key Laboratory of Advanced Materials (MOE), School of Materials Science and Engineering, Tsinghua University, Beijing, 100084, China

[b] Institut Lumière Matière, Université Claude Bernard Lyon 1, Villeurbanne, 69622, France

[c] CEMES-CNRS, Université de Toulouse, 29 rue J. Marvig, Toulouse, 31055, France

[d] School of Materials Science and Technology, Fujian University of Technology, Fuzhou, 350118, China

* Corresponding authors:

Jin-Yu Zhang, Email address: zhangjinyuchengqi@gmail.com

Wen-Zheng Zhang, Email address: zhangwz@tsinghua.edu.cn

Abstract

While the precipitation of α (hcp) from β (bcc) in various Ti alloys has been investigated in great detail, less is known about the precipitation of β from α. This study conducts a systematic investigation of structures and migrations of interfaces between β precipitates and α′ matrix in a Ti-2.6 wt% Mo alloy. Utilizing conventional and high-resolution transmission electron microscopy (TEM), assisted with molecular dynamics and generalized O-element analysis approaches, we unveil the dislocation and atomic structures of three typical portions of the interface surrounding a β precipitate, i.e., the habit plane, the side facet, and the end face. The habit plane of β precipitates contains two sets of dislocations with Burgers vectors $\mathbf{b}_1=[2\bar{1}\bar{1}3]_\alpha/6|[1\bar{1}1]_\beta/2$ and $\mathbf{b}_4=$

$[2\bar{1}\bar{1}\bar{3}]_\alpha / 6 | [11\bar{1}]_\beta / 2$, in contrast to the single set of $\mathbf{b}_1$ dislocations previously found on the habit plane of α laths precipitated from β matrix in various Ti alloys. Interface migrations during shrinkage of β precipitates are characterized via in-situ TEM, showing that both the habit plane and side facet migrate through the lateral motion of nanometer-high growth ledges. The dislocation structures of various growth ledges were obtained through generalized O-element calculations, suggesting a potential non-conservative dislocation trajectory as semicoherent growth ledges sweep across the interface.

Keywords: Interface structure; Interface migration; Titanium alloys; In-situ TEM; Molecular dynamics

1. Introduction

Titanium (Ti) alloys are pivotal in many important structural applications such as aerospace, shipbuilding, and biomedicine, owing to their superior specific strength, low-temperature performance, and corrosion resistance [1-4]. These properties are primarily attributed to the microstructure consisting of two allotropic forms of Ti: the hexagonal close-packed (HCP) α phase and the body-centered cubic (BCC) β phase. The transformation between these phases in different Ti alloys is a key determinant of the microstructures in the alloys, yielding various properties required by the applications of the alloys. Such a transformation proceeds through the generation and the migration of α/β interfaces, a process governed by the evolution of intricate interface

structures. Thus, a deep understanding of the α/β interface structures and their migration modes is essential, not only for comprehending the phase transformation kinetics in Ti alloys but also for advancing our ability to control the microstructure and design the titanium alloys.

The orientation relationship (OR) between α and β phases approximates the Burgers OR [5], namely

$$(0001)_\alpha \| (0\bar{1}1)_\beta ,\ [11\bar{2}0]_\alpha \| [111]_\beta . \quad (1)$$

The variant of the Burgers OR expressed by Eq. (1) is henceforth utilized throughout this study. Previous researches have extensively examined the interface structures surrounding α precipitates within the β matrix [6-14]. The α precipitate typically exhibits a lath morphology with a long axis and its interface consists of a pair of habit planes, side facets, and curved end faces. The habit plane is characterized by a single set of dislocation lines, while the side facet contains dual sets of parallel dislocations. The dislocations in these two portions of the interface all align parallel to the precipitate long axis. Using conventional transmission electron microscopy (TEM) [11] and high-angle annular dark-field scanning transmission electron microscopy (HAADF-STEM) [7, 8], the Burgers vectors of dislocations on the habit plane were identified as $\mathbf{b}_1 = [2\bar{1}\bar{1}3]_\alpha / 6 \,|\, [1\bar{1}1]_\beta / 2$ (<*c*+*a*>/2 type). Further TEM analysis [10] revealed the Burgers vectors of fine-spaced and coarse-spaced dislocations on the side facets as $\mathbf{b}_2 = [11\bar{2}0]_\alpha / 3 \,|\, [111]_\beta / 2$ (*a* type) and $\mathbf{b}_3 = [2\bar{1}\bar{1}0]_\alpha / 3 \,|\, [100]_\beta$, respectively. On the end face, a set of fine-spaced dislocation lines were observed by TEM [10] and high-resolution TEM studies [12, 13], with a Burgers vector of $\mathbf{b}_2$. Additionally, a dislocation

network composed of coarse-spaced segments was observed [6, 10], with TEM characterizations determining the Burgers vectors as $\mathbf{b}_1$, $\mathbf{b}_3$, and $\mathbf{b}_4 = [2\bar{1}\bar{1}\bar{3}]_\alpha / 6 \mid [11\bar{1}]_\beta / 2$ [6]. Complementing experimental findings, the interface dislocation structures of α precipitate were systematically simulated by molecular dynamics [15-17] and calculated by the generalized O-element approach [15, 18], with results that concur with experimental observations.

Yet, the migration mechanism of the α/β interface, particularly the motion of various interfacial dislocations, remains a subject of intrigue. Molecular dynamics simulations have been conducted to characterize the migration behavior of the semicoherent α/β interface [16, 19]. The simulations have revealed a shear-coupled interface migration mode associated with dislocation glide [19], corroborating the interface structure and the surface relief associated with α surface precipitates [20]. The α precipitate in bulk was suggested to grow through the motion of growth ledges, previously observed to be 10 nm in height [13]. Nevertheless, the detailed migration modes of the semicoherent α/β interfaces in the bulk, especially the intricate details of dislocation movements, were not reported.

In-situ TEM provides a potent avenue for probing the migration of α/β interfaces. However, the propensity of Ti to oxidize during in-situ heating poses a significant challenge to accurately characterizing this process. Given that oxygen diffusion is substantially lower in the α phase than in the β phase [21], studying the interface migration of β precipitates within an α matrix might be feasible, as supported by a relevant in-situ TEM study [22]. A further question of interest is how dislocations

intruding from the matrix may affect the crystallography of precipitates. This can be probed by comparing the interface structures generated in α precipitated from β and β precipitated from α, the latter of which is much less investigated. Flower et al. showed that β precipitates in Ti-Mo alloys align with near Burgers OR and the habit plane orientation [23] is similar to that of α precipitates [24]. Nonetheless, the detailed interface dislocation structures around β precipitates have not been thoroughly characterized, restricting a direct comparison of them with α precipitates.

This study conducts a systematic investigation of the β precipitate interfaces via TEM (Sections 3.1–3.4), complemented by molecular dynamics and geometric calculations (Sections 4.1 and 4.2), to reveal the three-dimensional (3D) interface dislocation structure. The in-situ TEM study investigates the migration modes of various α/β interfaces (Section 3.5), with a subsequent discussion on the potential evolution of interface structures during the migration (Section 4.3). Key conclusions are drawn together in Section 5.

2. Methodologies

2.1 Experimental setups

A Ti-2.6 wt% Mo alloy was selected for the experimental study in this work. A button ingot was obtained through vacuum arc melting and then forged in the β phase region into a bar with a size of 110 mm × 11 mm × 11 mm. For homogenizing composition, the sample was heated at 1100 ℃ for 3 days under an argon-protected environment, after a surface oxidation layer of 1 mm was removed. An additional 0.5 mm of the

surface layer was removed to avoid oxidized regions due to homogenization. The bar was then wire-cut into blocks of 8 mm × 8 mm × 5 mm. The alloy composition was determined with an X-ray fluorescence spectrometer (XRF-1800 X), revealing an alloy composition of 2.6 wt% Mo.

For heat treatment, the blocks were sealed in vacuum quartz tubes. Initially, they were solution-treated in the β phase region at 1100 ℃ for 30 minutes, followed by water quenching to room temperature to achieve an α′ martensitic structure. Subsequently, the blocks were resealed in vacuum quartz tubes and tempered at 670 ℃ for 24 hours followed by water quenching to room temperature to preserve the tempered microstructure. TEM samples for observations of interface structures were prepared by a preliminary mechanical thinning down to 40 μm and followed by ion thinning using a Gatan PIPS II. Interface characterizations under dark-field conditions were conducted using an FEI Tecnai G2 20 transmission electron microscope at 200 kV.

High-resolution characterizations of the interface structures were performed using samples prepared by the focused ion beam, with appropriate foil orientations determined by electron backscatter diffraction analysis before preparation. The high-resolution observations of the interfaces were carried out in a HAADF-STEM mode using a double aberration-corrected Titan Themis field emission transmission electron microscope at 300 kV.

To obtain samples for in-situ TEM observations, the same alloy was solution-treated at 1100 ℃ for half an hour and then water quenched to room temperature. The samples were then tempered at 670 ℃ for 6 hours to form β precipitates of a suitable size for in-

situ TEM study. TEM foils were prepared in the same way. In-situ TEM observations were performed under the microscope vacuum (typically 10^{-2} Pa) using a JEM2010 HC transmission electron microscope at 200 kV, employing a Gatan double-tilt heating holder. During the in-situ TEM study, the samples were first heated at 450 ℃. Then, the temperature was stepwisely increased by 50 K increments at an average rate of about 1 K/s and maintained for a few minutes in order to check possible interface migration. The temperature was eventually increased up to 950°C where fast interface motions were observed during several minutes.

2.2 Theoretical calculations

The theoretical determination of the preferred OR and habit plane structure between α′ and β phases is based on the O-lattice theory [25, 26] under the condition of the O-line criterion [27]. This criterion requires that the interfacial misfit across the habit plane be accommodated by a single set of dislocations, such that these dislocations alternate with the O-lines located at the centers of the coherent regions separated by the dislocations. The applicability of the O-line model has been substantiated through its successful explanation of α/β habit planes observed in previous experimental studies on Ti alloys [6, 11]. The Burgers vector of dislocations, acting as a key input, is determined based on the experimental observations (see Section 3.3). Since the O-line condition does not uniquely limit the OR [27], an additional constraint of the maximum dislocation spacing is applied, aligning with the previous study of Ti alloys [11]. The O-line calculation is performed using the software PTCLab designed for calculating

phase transformation crystallography [28]. The detailed calculation procedures using PTCLab for the present system are introduced in the Supplementary Materials.

Nevertheless, the O-line model does not apply to interfaces other than the habit plane. This limitation arises due to the absence of ideal O-lines—periodical locations where the misfit equals zero—between the dislocations in these interfaces. To circumvent this limitation, we employed the generalized O-element approach [18], which postulates the generalized O-elements, where the misfit attains local minima, as the centers of potential coherent zones on the interface. Using the OR determined by the O-line model as an input, a calculation based on the generalized O-lines can yield complicated dislocation structures across interfaces of various orientations. The congruence of this approach with both molecular dynamics simulations and experimental observations across diverse systems—including small angle grain boundaries, α/γ interfaces in duplex stainless steels, and interfaces surrounding α precipitates in Ti—underscores its robustness [15, 18]. The calculation details using the generalized O-element approach for the present system are elaborated in the Supplementary Materials.

2.3 Simulation setups

Molecular dynamics simulations are conducted to verify the interface dislocation structures predicted by geometric models. The atomic models of α′/β bicrystals are designed in alignment with the OR and interface orientations deduced from these geometric models. A refinement technique proposed in [29] is utilized to optimize initial configurations of the bicrystal model, to ensure that the irrational interfaces are virtually

devoid of interstitials and vacancies. Further details regarding the simulation setup, including the dimensions and orientations of the simulation box, are provided in the Supplementary Materials.

Initially, the bicrystal models are equilibrated under free boundary conditions at 300 K for 100 ps, followed by energy minimization using the fast inertial relaxation engine (FIRE) [30, 31]. We employed a state-of-the-art deep neural network potential [32, 33] recently developed for Ti-Mo alloys [19] to accurately describe the interactions between Ti and Mo atoms. The simulations are performed using the LAMMPS software [34, 35] in conjunction with the DeePMD-kit package [36, 37]. Given the negligible concentration of Mo in the α′ phase during precipitation due to its limited solubility, pure Ti is simulated for the α′ phase, with the lattice parameters a_α = 2.937 Å and c_α = 4.645 Å. The β phase, validated as stable at 300 K and 0 K for Mo compositions exceeding 10 at.% using the current potential, is examined at Mo concentrations of 10 at.%, 15 at.%, and 20 at.%. The results using the 20 at.% Mo β phase (the lattice parameter is a_β = 3.225 Å) are provided in details. Using this composition and the selected potential, the nano-sized α′ nuclei can be fully avoided in the random alloyed β phase after relaxation, which makes interface energy calculation feasible. The ratios of lattice parameters used in the simulation are consistent with those from the present experiment (a_α = 2.953 Å c_α = 4.682 Å, and a_β = 3.263 Å by X-ray diffraction) and from the previous studies [10, 11, 14, 24], where the spacing of habit plane dislocations of α precipitates is similar to that of β precipitates observed in the present work (Section 3.3). It is noted that all the simulated interfaces are immobile during the relaxation. The

crystal structures in the relaxed bicrystal models are identified using the Polyhedral Template Matching method [38] integrated in OVITO [39]. The positions and Burgers vectors of interface dislocations on the relaxed interfaces are characterized by a method [40] based on singular value decomposition of the Nye tensor [41]. In Table 1, we list the Burgers vectors of interface dislocations that may exist on the interfaces surrounding a β precipitate, as will be considered later. The notation is consistent with the previous study [15].

Table 1
Potential interface dislocations with Burgers vectors expressed in α′ and β phases.

Notations of dislocations	Burgers vectors in α′	Burgers vectors in β
$\mathbf{b}_1$	$[2\bar{1}\bar{1}3]_{\alpha'}/6$	$[1\bar{1}1]_{\beta}/2$
$\mathbf{b}_2$	$[11\bar{2}0]_{\alpha'}/3$	$[111]_{\beta}/2$
$\mathbf{b}_3$	$[2\bar{1}\bar{1}0]_{\alpha'}/3$	$[100]_{\beta}$
$\mathbf{b}_4$	$[2\bar{1}\bar{1}\bar{3}]_{\alpha'}/6$	$[11\bar{1}]_{\beta}/2$
$\mathbf{b}_5$	$[\bar{1}2\bar{1}0]_{\alpha'}/3$	$[\bar{1}11]_{\beta}/2$
$\mathbf{b}_6$	$[01\bar{1}\bar{1}]_{\alpha'}/2$	$[010]_{\beta}$
$\mathbf{b}_7$	$[01\bar{1}1]_{\alpha'}/2$	$[001]_{\beta}$

3. Experimental Results

3.1 Morphology

Fig. 1 characterizes α′ martensitic matrix and β precipitates at various magnifications, illustrating the microstructures at different spatial scales. As shown in Fig. 1(a), the optical micrograph (OM) displays a typical α′ martensitic morphology while the precipitates are too small to be visible. Fig. 1(b) shows a scanning electron micrograph

(SEM) after deep etching, where most of the β precipitates exhibit a lath-like morphology, with one dimension significantly longer than the others. This study primarily focuses on these predominant lath-like precipitates. In the TEM image of Fig. 1(c), the lath morphology of the β precipitates can also be observed. Multiple variants of the precipitates show a long-axis length of about 1 μm, which lies almost parallel to the surface of the TEM foil. Fig. 1(d) presents a bright-field image when the long axis of the precipitates is parallel to the electron beam direction, revealing that the precipitates are approximately 250 nm wide and about 50 nm thick. It is evident that the length of the long axis of the lath-like precipitate is substantially greater than its other two dimensions.

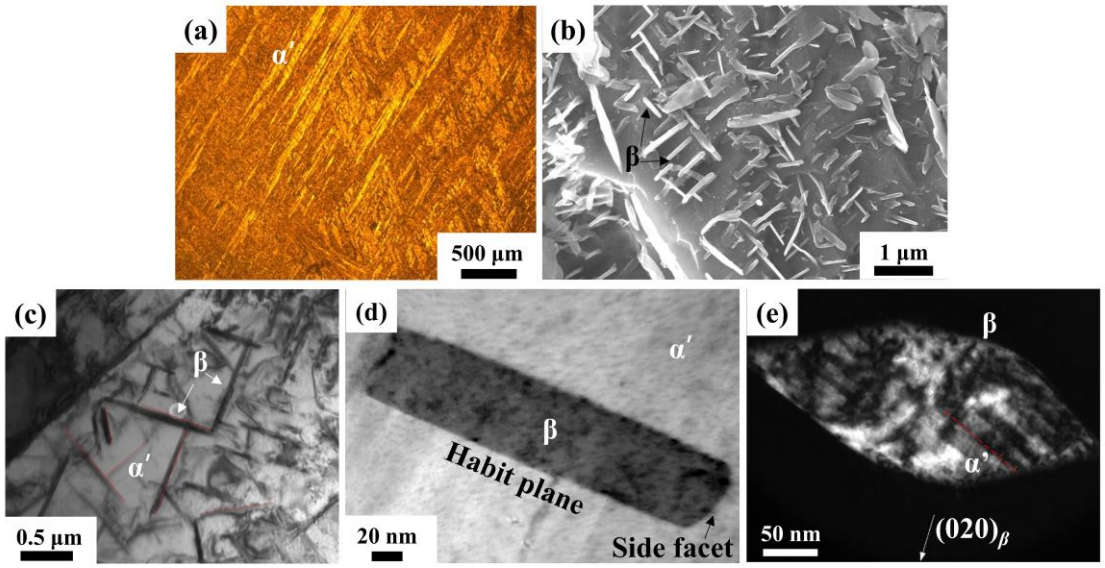

Fig. 1. Morphologies of β precipitates in α′ martensite tempered at 670 °C for 24 hours in a Ti-2.6 wt% Mo alloy, as observed under (a) OM; (b) SEM; (c) TEM image of different β precipitates; (d) Bright-field image of a β precipitate in an edge-on view; (e) Dark field image ($\mathbf{g} = (020)_{\beta}$) of a β precipitate, showing line contrast of

dislocations.

3.2 Orientation relationship, orientations of the long axis, and habit plane

The Kikuchi line method was utilized to precisely determine the OR between the β precipitates and their matrix. According to the determined three pairs of parallel unit vectors from the two phases, with these pairs being orthogonal to each other, an OR matrix was obtained to specify the OR between the two phases. The measured ORs are near an ideal Burgers OR ($(0001)_{\alpha'} \| (0\,\bar{1}\,1)_{\beta}$, $[11\bar{2}0]_{\alpha'} \| [111]_{\beta}$, and $[\bar{1}100]_{\alpha'} \| [\bar{2}11]_{\beta}$), as illustrated by $(0001)_{\alpha'}$, $[11\bar{2}0]_{\alpha'}$, and $[\bar{1}100]_{\alpha'}$ directions in a $[001]_{\beta}$ pole figure (Fig. 2(a)-(d)). The deviations of measured ORs from ideal Burgers OR are less than 1° and the averaged OR is expressed as: $(0001)_{\alpha'} \| (\overline{0.0022}\ \ \overline{1.0043}\ \ 1)_{\beta}$ with a deviation angle of 0.6° from $(0\,\bar{1}\,1)_{\beta}$, $[11\bar{2}0]_{\alpha'} \| [1.01\ \ 1\ \ 1.01]_{\beta}$ with a deviation angle of 0.4° from $[111]_{\beta}$.

The orientations of habit planes of β precipitates were determined using the software τompas [42], an integrated tool for crystallographic analysis of TEM images. By obtaining the projection widths and traces of the interfaces at various beam directions, the habit plane orientations of β precipitates were solved, as shown in Fig. 2(a) and (e). The measured orientations fluctuate within approximately ±5°, all being irrational planes with an average of $(\overline{1.4}\ \ 1.1\ \ 1.0)_{\beta} \| (\overline{4.0}\ \ 5.0\ \ \overline{1.0}\ \ \overline{0.29})_{\alpha'}$. The long axis of the precipitates was characterized by the line directions of dislocations on the habit plane (Fig. 1(e)), as suggested in the previous studies [11, 24]. Fig. 2(f) shows the measured orientations by trace analysis, with an average of $[1.8\ \ 1.0\ \ 1.2]_{\beta} \| [2.7\ \ 1.0\ \ \overline{3.7}\ \ 0.16]_{\alpha'}$

and a fluctuation of about ±6°. The orientations of habit plane and long axis measured in the present study are close to the ones observed in α precipitates in Ti-Cr alloys [11, 13, 24].

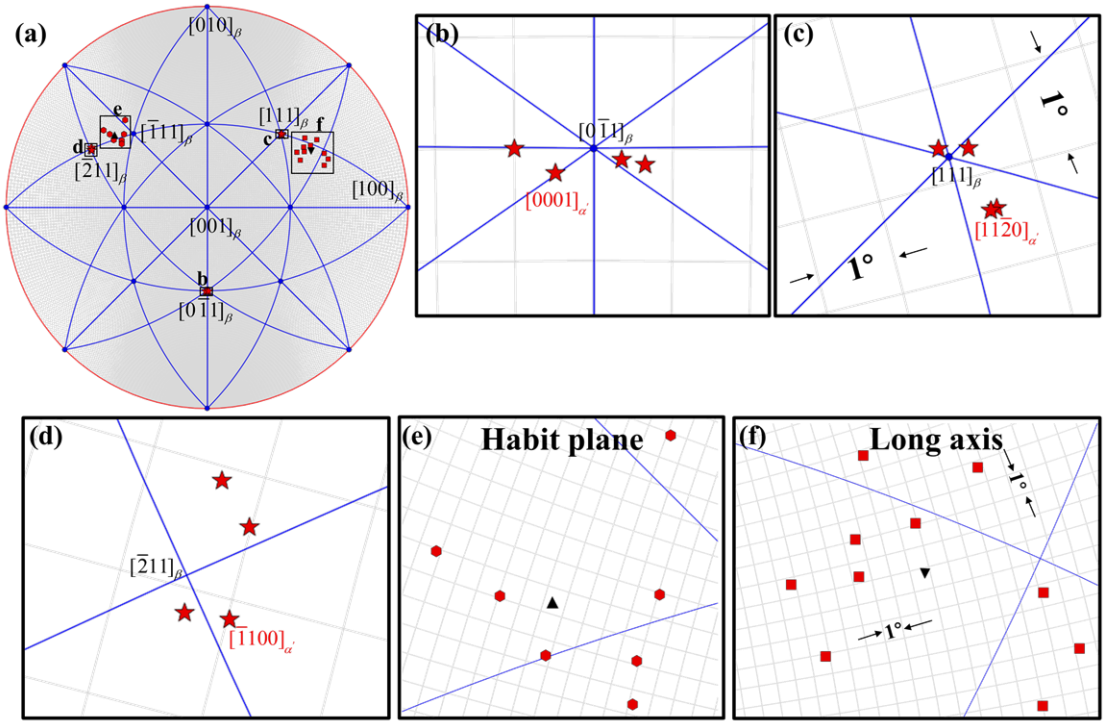

Fig. 2. Illustration of the measured ORs, the habit plane normals, and the long axis directions of β precipitates in a $[001]_\beta$ polar figure. (b)-(f) are enlarged figures of boxed areas in (a). ☆ symbols in (b), (c), and (d) represent $[0001]_{\alpha'}$, $[11\bar{2}0]_{\alpha'}$, and $[\bar{1}100]_{\alpha'}$ orientations in the matrix near the measured precipitates. In (e) and (f), red hexagons and squares are measured orientations of habit plane normals and long axis directions, respectively, for different precipitates, and black triangles indicate the average directions.

3.3 Interface structure of the habit plane

Fig. 3 presents HAADF-STEM images of habit planes of a β precipitate viewed along $[0\bar{1}1]_{\beta}|[0001]_{\alpha'}$. In Fig. 3(a), the habit plane is seen almost edge-on, consistent with its orientation $(\overline{1.4}\ 1.1\ 1.0)_{\beta}\|(\overline{4.0}\ 5.0\ \overline{1.0}\ \overline{0.29})_{\alpha'}$ approximately containing $[0\bar{1}1]_{\beta}|[0001]_{\alpha'}$ directions. Fig. 3(b) reveals that the interface is composed of atomic steps, a structure that aligns with reports by previous studies [8, 9, 13]. The steps, whose height corresponds to twice the atomic spacing between $(\bar{2}200)_{\alpha'}|(\bar{2}11)_{\beta}$ planes, are irregularly spaced. They were referred to as structural ledges [13] or disconnections [8]. Across the entire interface region of the habit plane observed in this zone axis in TEM, no dislocations were detected (in Fig. 3). This is because the dislocations are almost parallel to the trace of the habit plane viewed at this beam direction of $[0\bar{1}1]_{\beta}|[0001]_{\alpha'}$, to which the dislocation line direction $[1.8\ 1.0\ 1.2]_{\beta}$ is nearly vertical.

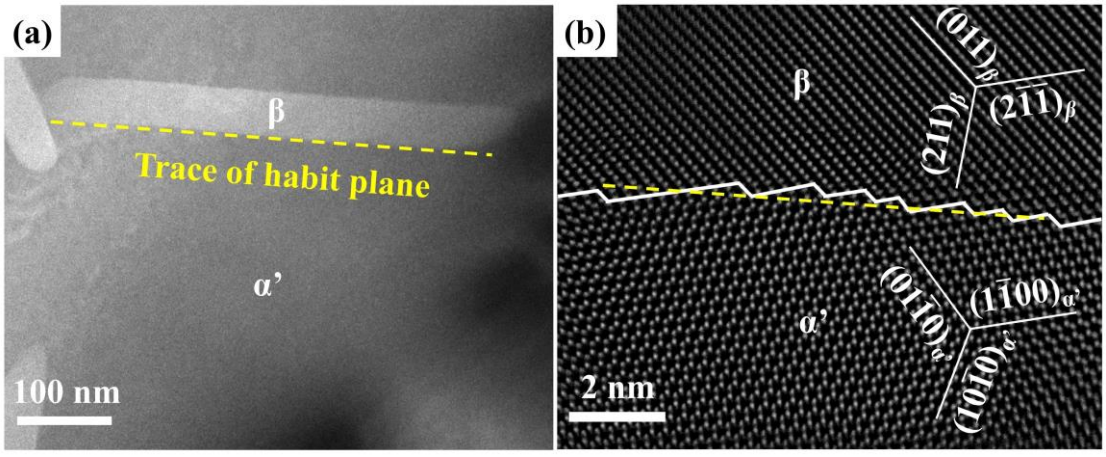

Fig. 3. HAADF-STEM image of the habit plane of a β precipitate within α′ martensite of a Ti-2.6 wt% Mo alloy tempered at 670 ℃ for 24 hours. (a) A low-magnification image of edge-on habit planes; (b) A high-resolution image captured from $[0\bar{1}1]_{\beta}|[0001]_{\alpha'}$ direction.

The structure of the habit plane has been examined from another direction, $[111]_{\beta}$ | $[11\bar{2}0]_{\alpha'}$ with high-resolution TEM. Fig. 4 shows the high-resolution images from the boxed area in Fig. 4(a). Two types of dislocations with different Burgers vectors were observed on the habit plane viewed from the beam direction of $[111]_{\beta}$ | $[11\bar{2}0]_{\alpha'}$. The in-plane components of these two types of Burgers vectors were determined using Burgers circuit analysis, as magnified in Fig. 4(c), and (d). Under this zone axis, the adjacent atomic columns are linked by three $<112>_{\beta}/3$ vectors, i.e., $\mathbf{v}_1 = [1\bar{2}1]_{\beta}/3$, $\mathbf{v}_2 = [11\bar{2}]_{\beta}/3$, and $\mathbf{v}_3 = [\bar{2}11]_{\beta}/3$. The projections of the possible Burgers vectors in Table 1 in the direction of $[111]_{\beta}$ are listed in Table 2, to compare with the measured in-plane component of the Burgers vectors. According to the Burgers circuits in Fig. 4(c) and (d), the two types of in-plane components of the Burgers vectors are $\mathbf{v}_1$ and $\mathbf{v}_2$, respectively. From Table 2, the Burgers vectors of the dislocations on the habit plane could be either of the $<1\bar{1}1>_{\beta}/2$ | $<2\bar{1}\bar{1}3>_{\alpha'}/6$ ($\mathbf{b}_1$ or $\mathbf{b}_4$) type or $<010>_{\beta}$ | $<01\bar{1}\bar{1}>_{\alpha'}/2$ type ($\mathbf{b}_6$ or $\mathbf{b}_7$). Thus, the information from the above high-resolution TEM study is insufficient to define the Burgers vectors of the dislocations.

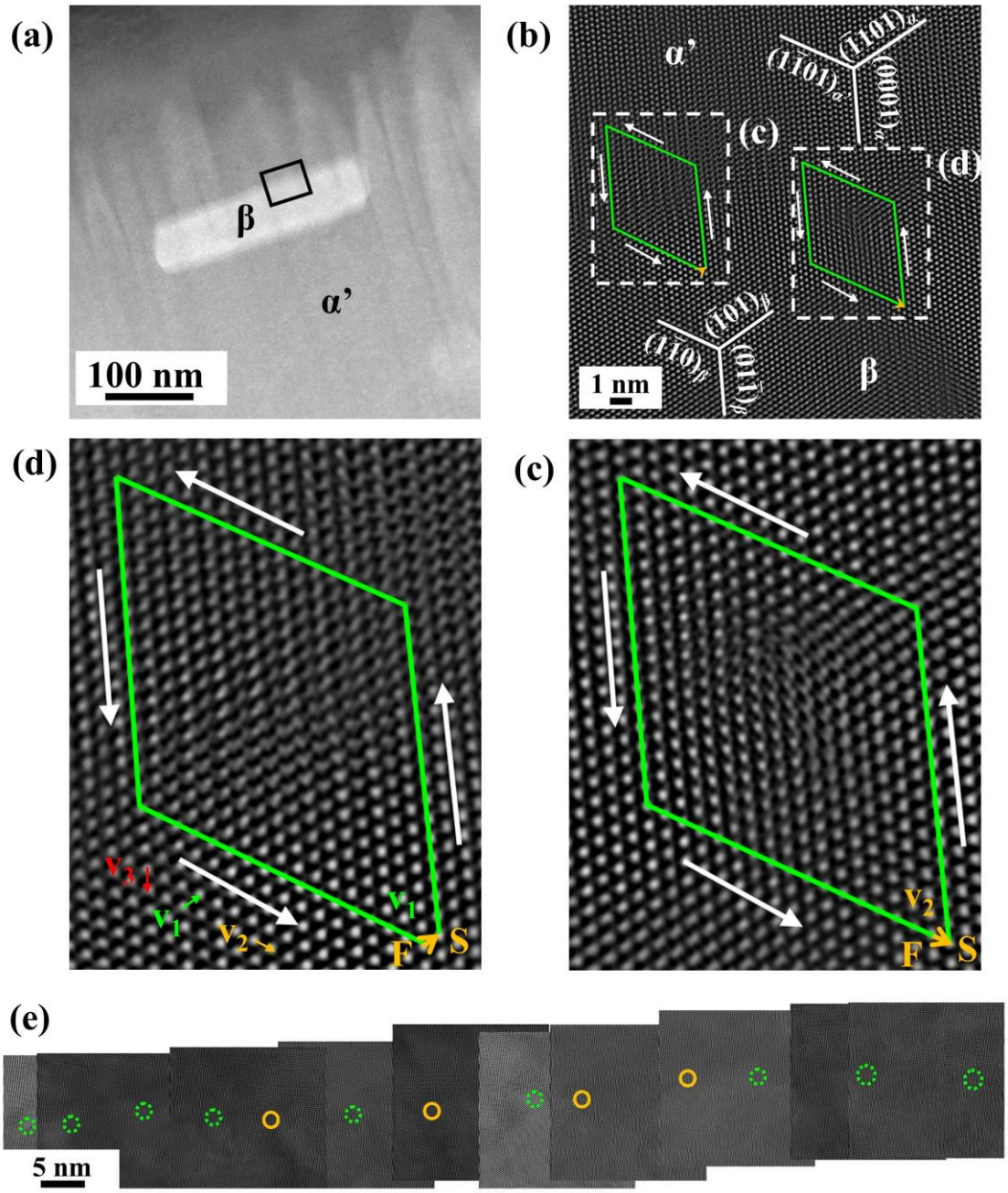

Fig. 4. Dislocation structures of habit plane of a β precipitate in α′ martensite tempered at 670 °C for 24 hours viewed from $[111]_{\beta}\,|\,[11\bar{2}0]_{\alpha'}$. (a) low-magnification image and (b)–(e) HAADF-STEM high-resolution micrographs. (c) and (d) are magnifications of the boxed areas in (b), showing detailed structures. (e) depicts the dislocations across an entire habit plane of the β precipitate, with the positions of the interface dislocation cores marked by circles. Green segments represent the Burgers circuits around the

dislocations. Yellow solid and green circles represent the core positions of dislocations with two different types of Burgers vectors.

Table 2
Projected vectors along $[111]_\beta \,|\, [11\bar{2}0]_{\alpha'}$ and **g**·**b** results for different possible Burgers vectors

Burgers vectors	Projected vectors	**g**·**b** for different **g**'s			
		$\mathbf{g}=(011)_\beta$	$\mathbf{g}=(020)_\beta$	$\mathbf{g}=(002)_\beta$	$\mathbf{g}=(0\bar{1}1)_\beta$
$\mathbf{b}_1=[1\bar{1}1]_\beta/2\,\|\,[2\bar{1}\bar{1}3]_{\alpha'}/6$	$\mathbf{v}_1$	0	-1	1	1
$\mathbf{b}_2=[111]_\beta/2\,\|\,[11\bar{2}0]_{\alpha'}/3$	**0**	1	1	1	0
$\mathbf{b}_3=[100]_\beta\,\|\,[2\bar{1}\bar{1}0]_{\alpha'}/3$	$\mathbf{v}_3$	0	0	0	0
$\mathbf{b}_4=[11\bar{1}]_\beta/2\,\|\,[2\bar{1}\bar{1}3]_{\alpha'}/6$	$\mathbf{v}_2$	0	1	-1	-1
$\mathbf{b}_5=[\bar{1}11]_\beta/2\,\|\,[\bar{1}2\bar{1}0]_{\alpha'}/3$	$\mathbf{v}_3$	1	1	1	0
$\mathbf{b}_6=[010]_\beta\,\|\,[01\bar{1}\bar{1}]_{\alpha'}/2$	$\mathbf{v}_1$	1	2	0	-1
$\mathbf{b}_7=[001]_\beta\,\|\,[01\bar{1}1]_{\alpha'}/2$	$\mathbf{v}_2$	1	0	2	1

To complete the characterization of the Burgers vectors of these dislocations, dislocation contrast analysis was applied under different **g** conditions. Fig. 5 shows various dislocation contrasts in various TEM images. Using $\mathbf{g}=(011)_\beta$, the dislocation contrast on the habit plane is quite weak, with the dislocations on the habit plane of the precipitate in the boxed area in Fig. 5(a) almost completely extinguished. The very weak contrast with $\mathbf{g}=(011)_\beta$ suggests that **g**·**b** = 0. On the contrary, under the other three **g** conditions, i.e., $\mathbf{g}=(020)_\beta$, $\mathbf{g}=(002)_\beta$, and $\mathbf{g}=(0\bar{1}1)_\beta$, the contrast of interface dislocation is stronger. From Table 2, the **g**·**b** analysis suggests that the Burgers vectors belong to the $<1\bar{1}1>_\beta/2\,|\,<2\bar{1}\bar{1}3>_{\alpha'}/6$ (**b**$_1$ or **b**$_4$) type rather than $<010>_\beta\,|\,<01\bar{1}\bar{1}>_{\alpha'}/2$ type (**b**$_6$ or **b**$_7$). Therefore, a combination of the results of the

contrast analysis with conventional TEM and the Burgers circuits based on the high-resolution TEM images concludes that the two types of dislocations in the habit plane are associated with the Burgers vectors of $\mathbf{b}_1=[1\bar{1}1]_\beta/2|[2\bar{1}\bar{1}3]_{\alpha'}/6$ and $\mathbf{b}_4=[11\bar{1}]_\beta/2|[2\bar{1}\bar{1}\bar{3}]_{\alpha'}/6$. This type of Burgers vector is consistent with the conclusions from the previous study of α precipitates in Ti alloys [8, 11]. However, in the present study of β precipitates, two types of $<1\bar{1}1>_\beta/2|<2\bar{1}\bar{1}3>_{\alpha'}/6$ dislocations coexist on the habit plane instead of only one type in the previous works. These two Burgers vectors are symmetric about the *c*-plane of the HCP lattice. The analysis of the dislocations across the entire habit plane of a precipitate is shown in Fig. 4(e). It can be seen that the two types of dislocations are distributed in roughly uniform spacing, with a ratio of approximately 2:1 for $\mathbf{b}_1$ and $\mathbf{b}_4$. They constitute the parallel dislocations on the habit plane observed in the low-magnification dark-field image.

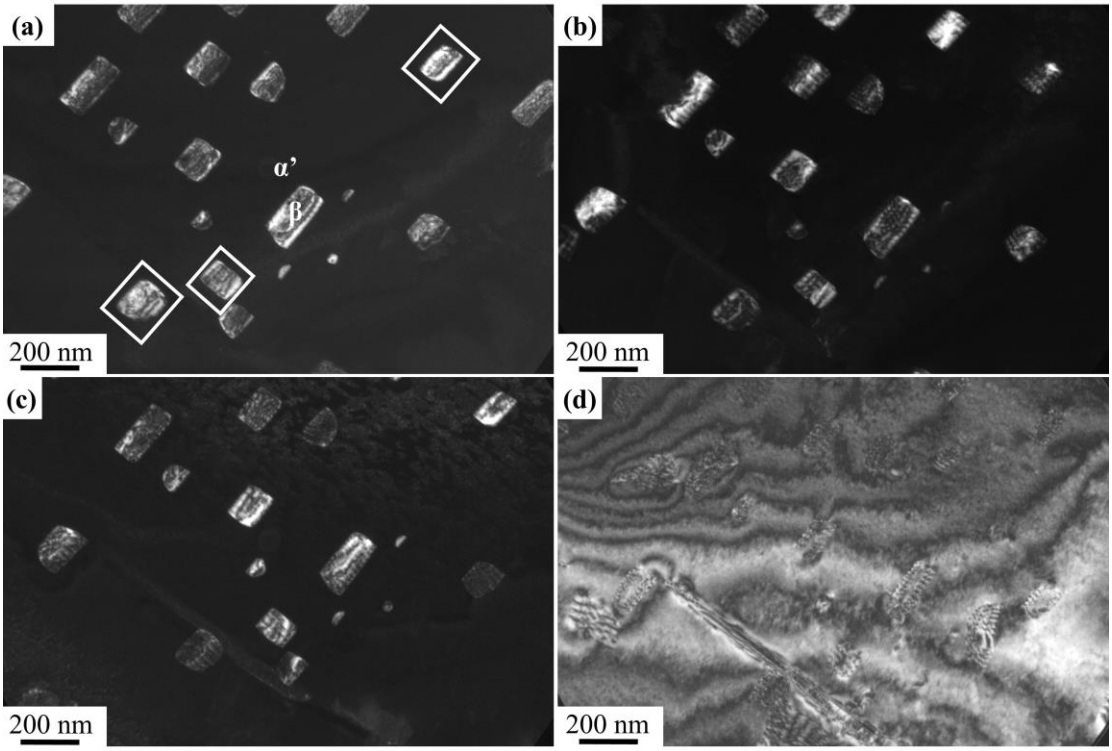

Fig. 5. Dark-field images of β precipitates in α′ martensite tempered at 670 ℃ for 24 hours under different **g** conditions. (a) $\mathbf{g} = (011)_{\beta}$, (b) $\mathbf{g} = (020)_{\beta}$, (c) $\mathbf{g} = (002)_{\beta}$, (d) $\mathbf{g} = (0\bar{1}1)_{\beta}$

3.4 Interface structure of the side facet and the end face

Fig. 6 is a dark-field image of the interfaces using $\mathbf{g} = (10\bar{1}\bar{1})_{\alpha'}$. Though the contrast of the parallel linear defects in the broad interface is significant, fine-spaced dislocations on the side facet are visible by careful inspection, especially in the regions marked by boxes. The dislocation structure of the side facet was characterized at the atomic scale, with high-resolution HAADF-STEM imaging using the precipitate in Fig. 4(a). Fig. 7(a) shows one set of dislocations, with a projected dislocation spacing of ~8.5 nm. The Burgers vector of these dislocations was analyzed using the Burgers circuit (Fig. 7(b)), with its projection component being $\mathbf{v}_3 = [\bar{2}11]_{\beta}/3$. According to Table 2, the possible Burgers vector is either $\mathbf{b}_3=[100]_{\beta}|[2\bar{1}\bar{1}0]_{\alpha'}/3$ or $\mathbf{b}_5=[\bar{1}11]_{\beta}/2|[\bar{1}2\bar{1}0]_{\alpha'}/3$, which are *a*-type dislocations in HCP. Considering that the weak but persistent contrast of dislocations with $\mathbf{g} = (10\bar{1}\bar{1})_{\alpha'}$ in Fig. 6, the plausible Burgers vector of the dislocations is $\mathbf{b}_3= [100]_{\beta} | [2\bar{1}\bar{1}0]_{\alpha'}/3$. This set of dislocations is consistent with a previous TEM characterization of the coarse-spaced dislocations on the side facet of α precipitates in a Ti-7.26 wt% Cr alloy [10], while the atomic image of this set of dislocation was not reported before.

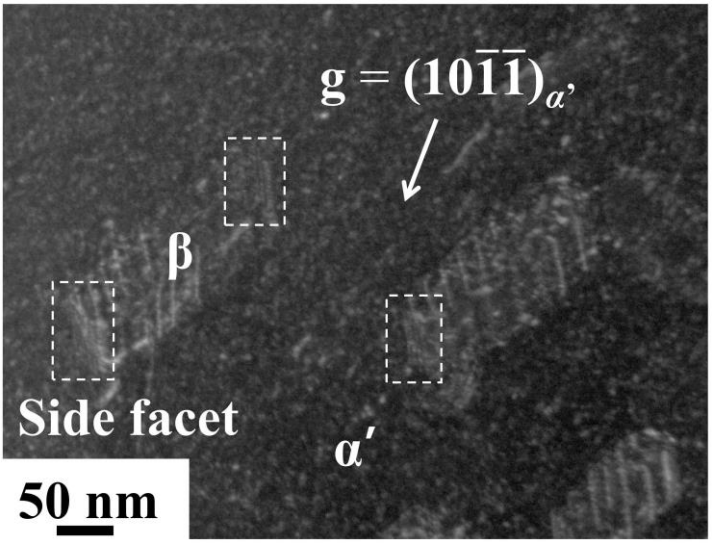

Fig. 6. A dark-field image ($\mathbf{g} = (10\bar{1}\bar{1})_{\alpha'}$) of the β precipitates in α′ martensite tempered at 670 ℃ for 24 hours. The side facets are marked by boxes.

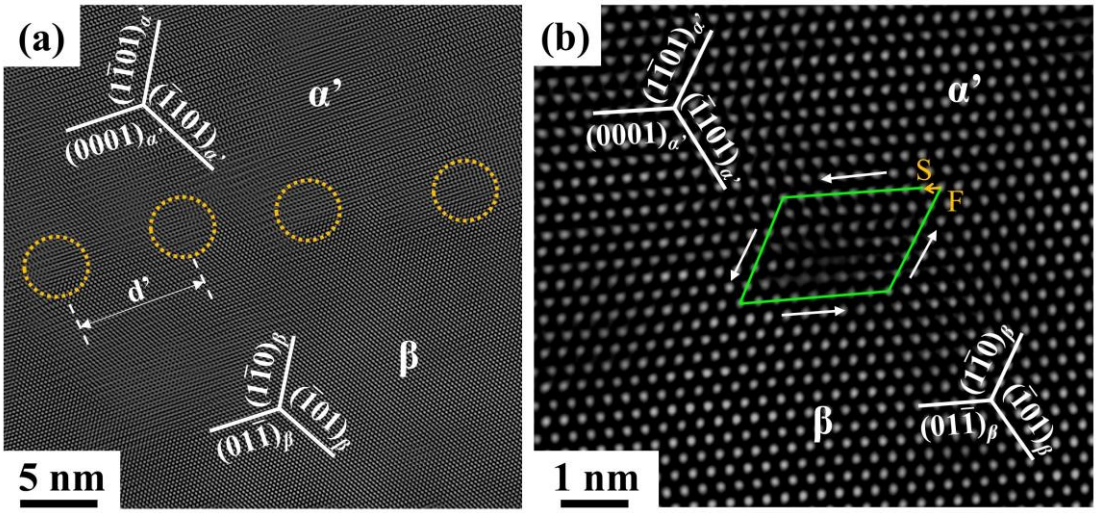

Fig. 7. HAADF-STEM images of the side facet of a β precipitate in α′ martensite tempered at 670 ℃ for 24 hours, under $[111]_{\beta}\,|[11\bar{2}0]_{\alpha'}$ zone axis. (a) high-resolution image of the side facet on the right in Fig. 4(a); (b) Burgers circuit analysis of one dislocation in (a).

The apparent "side faces" of β precipitates are also characterized from a foil nearly parallel to $(0\bar{1}1)_\beta \,|\, (0002)_{\alpha'}$. Since the long axis approximately lies in $(0\bar{1}1)_\beta \,|\, (0002)_{\alpha'}$, the "side face" of a β precipitate in this orientation is actually the end face (or tip) of the β precipitate, as illustrated schematically in Fig. 8(a). The boxed area in Fig. 8(b) is characterized using HAADF-STEM imaging. Fig. 8(c) is from a transition zone from the habit plane to the end face. It shows a series of nanometer-high ledges, each of which is associated with a dislocation. With an enlarged image as in Fig. 8(d), the Burgers vector of these dislocations can be identified as $\mathbf{b}_2=[111]_\beta/2\,|\,[11\bar{2}0]_{\alpha'}/3$, as marked by $\mathbf{t}_1$ in Fig. 8(e). This set of dislocations is consistent with the previous observations of α precipitates (Fig. 4(a) in Ref. [13] and Figure 5 in Ref. [12]), while the atoms on $(011)_\beta$ planes were not resolved in the previous studies. When the interface orientation significantly deviates from the habit plane, another type of dislocations is identified by a careful examination. The Burgers circuit analysis indicates that these dislocations are associated with a Burgers vector with a projected vector of $\mathbf{t}_4 = [100]_\beta/2\,|\,[2\bar{1}\bar{1}0]_{\alpha'}/6$, as shown in Fig. 8(f). The possible Burgers vector of this dislocation is either $\mathbf{b}_1=[1\bar{1}1]_\beta/2\,|\,[2\bar{1}\bar{1}3]_{\alpha'}/6$ or $\mathbf{b}_4=[11\bar{1}]_\beta/2\,|\,[2\bar{1}\bar{1}\bar{3}]_{\alpha'}/6$.

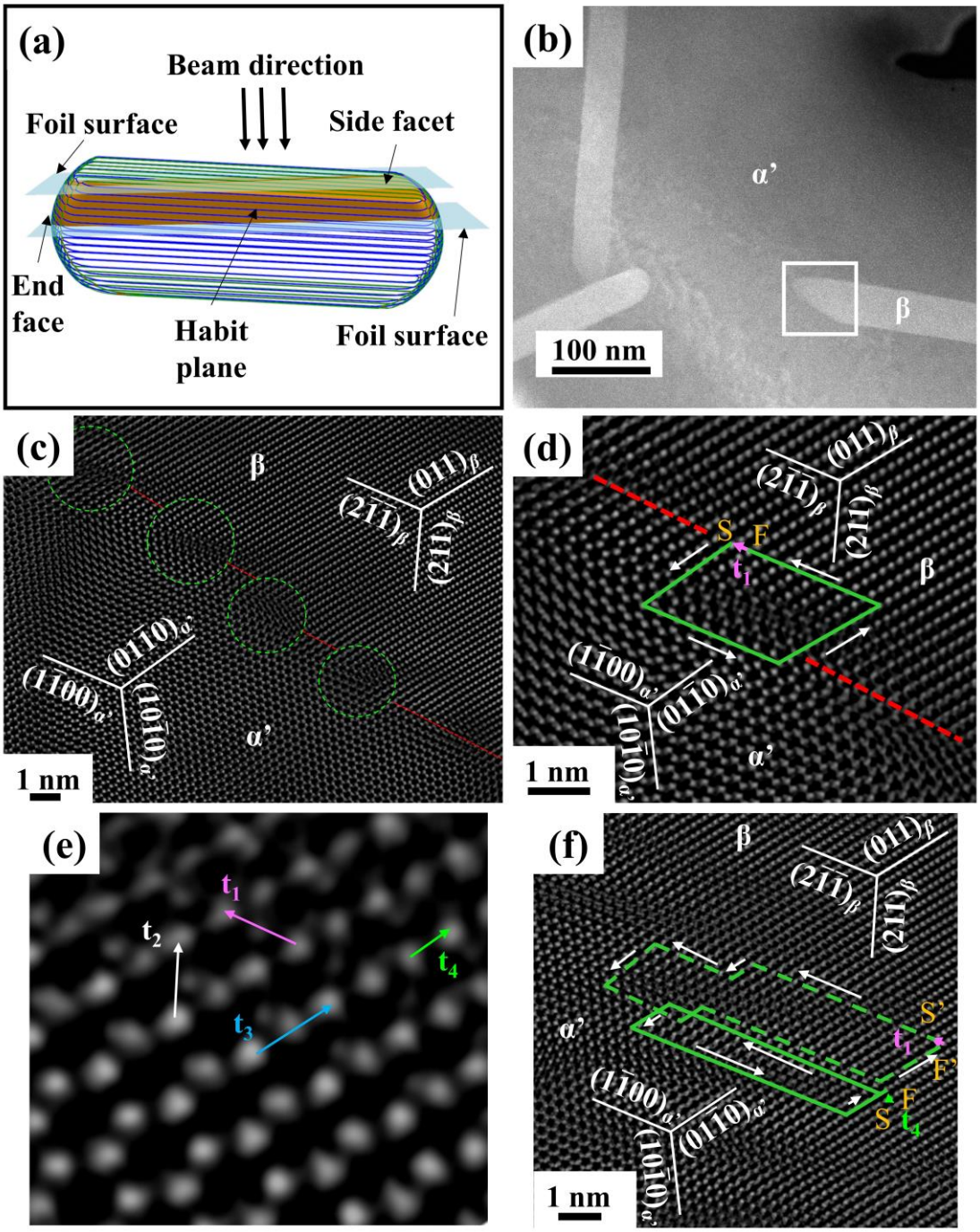

Fig. 8. HAADF-STEM images of the end face of β precipitates in α′ martensite tempered at 670 °C for 24 hours, under $[0\bar{1}1]_{\beta}|[0001]_{\alpha'}$ zone axis. (a) Schematics of the foil normal and interfaces around the precipitate; (b) low-magnification image; (c) periodic fine-spaced dislocations (inside circles), where red dashed lines are approximate positions of terraces; (d) Burgers circuit analysis of dislocations in (c);

(e) Possible projected lattice vectors under this zone axis; (f) Burgers circuit analysis of two types of dislocations on the end face.

3.5 In-situ TEM observation of interface migration mode

All β precipitates remain unchanged during in-situ heating until the indicated temperature reaches 800 ℃. At the higher temperatures and even above the β transus (about 860 ℃ for this alloy), most precipitates are still unchanged, but a few β precipitates were found to shrink. A possible reason for those precipitates to remain unchanged is that the interfaces between the precipitates and matrix are pinned by the foil surface. The few shrinkable precipitates may be coincidently embedded within the TEM foil, such that the interface motion is not pinned. According to the phase diagram for the alloy, the β precipitates are expected to grow with increasing temperature at this temperature range. However, the composition change of the alloy due to heating in the atmosphere conditions in TEM may affect the stability of β. For example, possible absorption of oxygen may stabilize the α matrix [43]. It is also possible that the interface movement process is driven by the interface tension. However, such a process must involve precipitate growth, which was not observed. This may be due to a kinetical reason because the barrier to shrinking is likely smaller than to growing of β precipitates. The growth of β precipitates requires new interfacial defects to be added to the interfaces of increasing size. In contrast, migration of interfaces during shrinkage of β precipitates only involves the movement of existing interfacial defects. The barrier to starting the movement of unpinned existing interfacial defects is expected to be much

lower compared to that needed for the nucleation of various interfacial defects.

The shrinkage process of a β precipitate was recorded at a temperature of 950 ℃ for the sample hot stage. Fig. 9 displays the snapshots of this process, in which the shrinking β precipitate is pointed by an arrow. The migration of the interface surrounding this precipitate exhibits anisotropic kinetics, with the interfaces maintaining consistent orientations throughout the process: The broad facet marked by 'A' is hardly mobile until the last seconds when the precipitate rapidly shrinks and vanishes (Fig. 9(e) and (f)). The shrinkage of the β precipitate proceeds mainly through the prominent migration of the interface portion marked by 'B', which is likely the end face since it is normal to the line defects visible in the broad facets of several β precipitates with the same direction of the long axis. To verify the types of interfaces at 'A' and 'B' portions in the in-situ study (Fig. 10(a)), a similar precipitate in Fig. 10(b) was characterized in a nearby area after the in-situ heating experiment. By comparing the diffraction spots and morphology of the precipitates and the matrix in Fig. 10(a) with those in Fig. 10(b), they appear highly similar, sharing the same variant of the OR. According to the observation of the parallel dislocation lines and measurement of the interface at portion 'A', i.e., $(\overline{1.3}\ 1.3\ 1.0)_{\beta}$, it is confirmed that the interface at portion 'A' is the habit plane and the interface at portion 'B' is the end face.

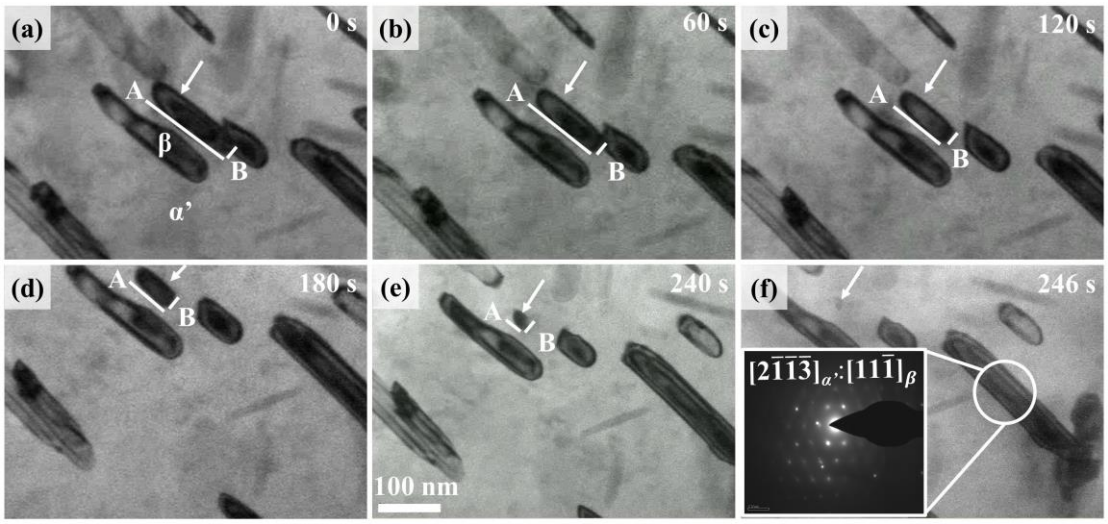

Fig. 9. Shrinkage of a β precipitate during in-situ heating. (a) t = 0 s; (b) t = 60 s; (c) t = 120 s; (d) t = 180 s; (e) t = 240 s; (f) t = 246 s. In (f), the diffraction pattern of a similar precipitate near the vanished one shows $[11\bar{1}]_{\beta}$ and $[2\bar{1}\bar{1}\bar{3}]_{\alpha'}$ zone axes.

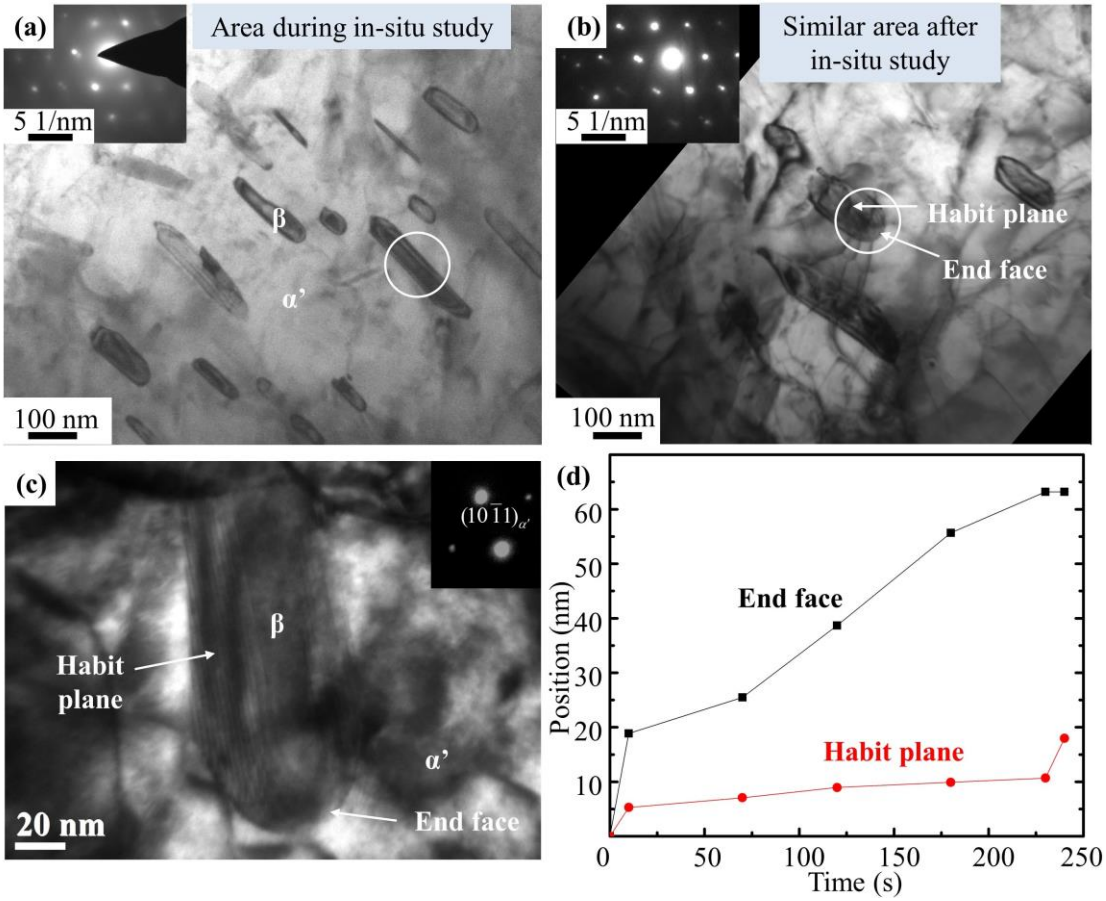

Fig. 10. (a) Bright-field image of the area observed in-situ and the diffraction pattern in

the circled area; (b) Bright-field image of a similar area after in-situ study and diffraction patterns resembling those of the precipitate and matrix in (a); (c) Enlarged morphology of the precipitate marked with a circle in (b); (d) The corrected migration distance with time for the two interfaces of the shrinking precipitate in Fig. 9.

The migration distance of the two interfaces with the projection effect corrected is shown in Fig. 10(d). Before 220 s, the migration rates of the habit plane and the end face are 2.8 nm/min and 17.3 nm/min, respectively. The precipitate transformed from a lath-like to a block-like shape due to the faster migration of the end face. Subsequently, the block-like precipitate rapidly contracted and vanished from all directions.

The anisotropy of interface migration rates can be understood from the different migration modes of the interface, in conjunction with the dislocation structures in the different portions of the interface. While the end face is likely to move continuously, the faceted interfaces cannot be so, as manifested by careful examination of dynamic details of the defect structure in the interface surrounding a β precipitate during in-situ heating. Coincidently, the end face of this β precipitate does not quickly move for an unknown reason, giving a chance to observe the migration mode of different facets that contain the parallel defects along the long axis. Both facets are not seen to move continuously along their normal. In addition, the parallel defects were not found to move continuously normal to the line direction either. The migrations of these facets are possibly caused by the lateral motion of the growth ledges with these facets as the terrace planes of the ledges. Fig. 11 shows bright field snapshots taken during heating

(refer to the Supplementary Movie for more details). One can see various defects with dark contrasts that are free to move along the long axis of the precipitate. For example, a pair of defects indicated by arrows in Fig. 11 starts from locations near both end faces at different sites. These defects already exist in the interface, which are possibly growth ledges associated with dislocations as seen in Fig. 8(c). The growth ledges move toward each other along the facet (called Facet 1) and eventually annihilate when they meet each other. The lateral motion of these growth ledges results in movement of the Facet 1 towards the β precipitate, leading to its shrinkage.

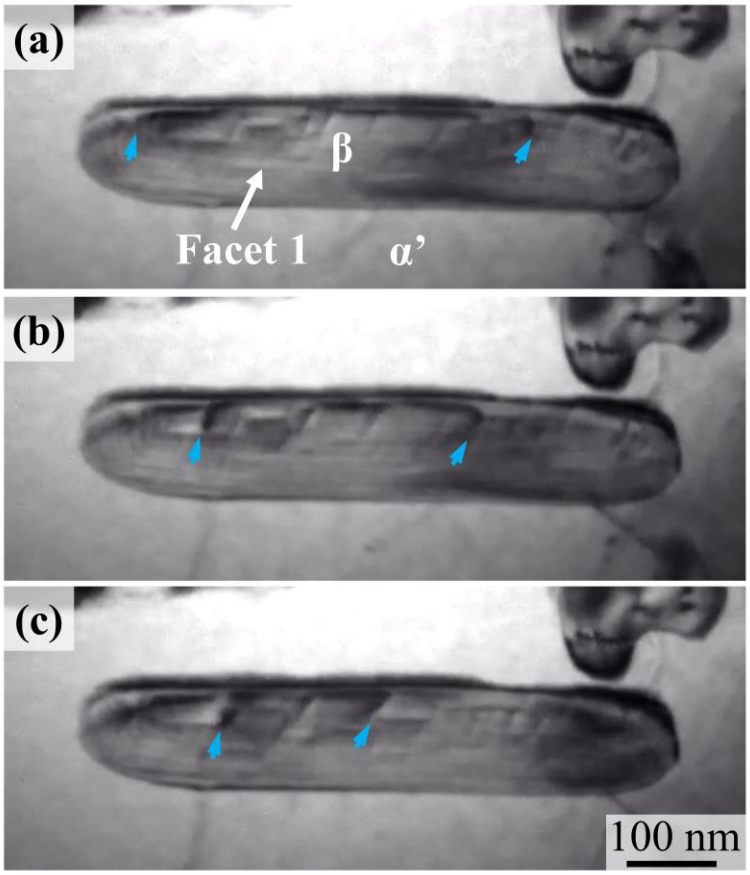

Fig. 11. Motion of linear defects and growth ledges on Facet 1 of a β precipitate during the in-situ heating at (a) 155 s, (b) 165 s, and (c) 190 s in the Supplementary

Movie. Blue arrows in (a) to (c) point to two growth ledges from opposite directions on Facet 1.

Similar to the motion of observed defects on Facet 1, migration of growth ledges on another further inclined facet (Facet 2) was also observed. The ledges near the top of the precipitates are often associated with a strong contrast, as marked by a set of arrows. These are not edge-on ledges, as they are connected to and move together with linear defects in Facet 2. Therefore, the linear movable defects are likely also ledges. These ledges likely form loops in Facet 2, though the contrast of complete ledge loops is faint. As shown in Fig. 12, growth ledges on the Facet 2 primarily emerge near the end face (refer to the Supplementary Movie). For example, at 35 s, the growth ledge, marked as "1" in the figure, emerges from the end face on the right side and then migrates to the left at 45 s and disappears near the opposite end face. Meanwhile, more growth ledges are consecutively emitted from the end face on the right side, marked as "2" to "5" in the figure. The average migration rate of growth ledges 1, 2, and 3 in Fig. 12 are 8.9 nm/s, 8.1 nm/s, and 8.3 nm/s, respectively, yielding an average lateral migration rate of 8.4 nm/s. In contrast to the rather smooth migration along the long axis of the precipitates, the overall shapes of the visible ledges are not characterized by smooth curvature. The ledges tend to lie along the long axis of the precipitates, leading to kinked contrast as seen in Fig. 12(b). It suggests the difficulty for the ledge to migrate in the direction normal to the periodic misfit field in the facet (Fig. 8 (a)). This observation verifies a terrace-ledge-link model suggested in a previous investigation [13].

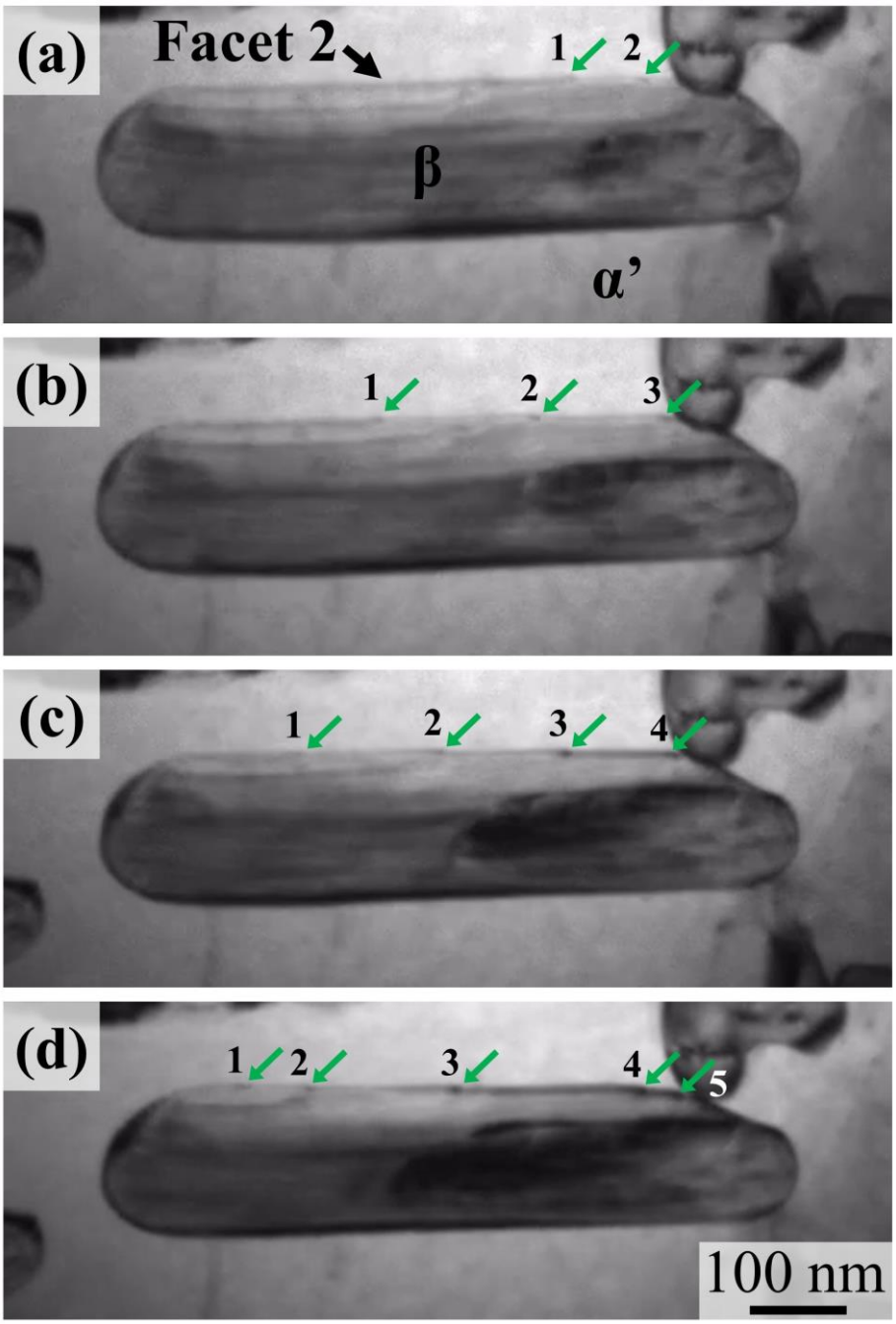

Fig. 12. Emission of growth ledges on Facet 2 from the end face of a β precipitate and their lateral motion at (a) 25 s, (b) 35 s, (c) 45 s, and (d) 57 s in Supplementary Movie. Green arrows point to growth ledges on Facet 2.

The annihilation of growth ledges on Facet 2 is elucidated in further detail in Fig. 13.

As seen in Fig. 12, the ledges in pairs, e.g., 3 and 3’ or 4 and 4’, move toward the opposite direction, though ledges 3’ and 4’ are much less mobile than ledge 3 and 4. The ledges in the same pair possibly initiated from the end faces at different sides. The terrace planes of these ledges are all parallel to Facet 2 and they probably carry the same types of dislocations. Because the normals of the ledge risers have the opposite direction, the signs of Burgers vectors are also opposite. Consequently, when ledge 3 meets ledge 3’ near the end face on the left side, the dislocations associated with the ledges annihilate together with the disappearance of the ledges, as shown in Fig. 13(d). The same process possibly occurs for ledge pair marked by 4 and 4’, bounded by a faint curved line contrast. The in-situ observation of ledge motions, as shown in Fig. 12 and Fig**. 13**, and Supplementary Movie, evidently indicates the migration of Facet 2 toward β and hence the shrinkage of the β precipitate via a process of emission, lateral motion, and annihilation of the growth ledges.

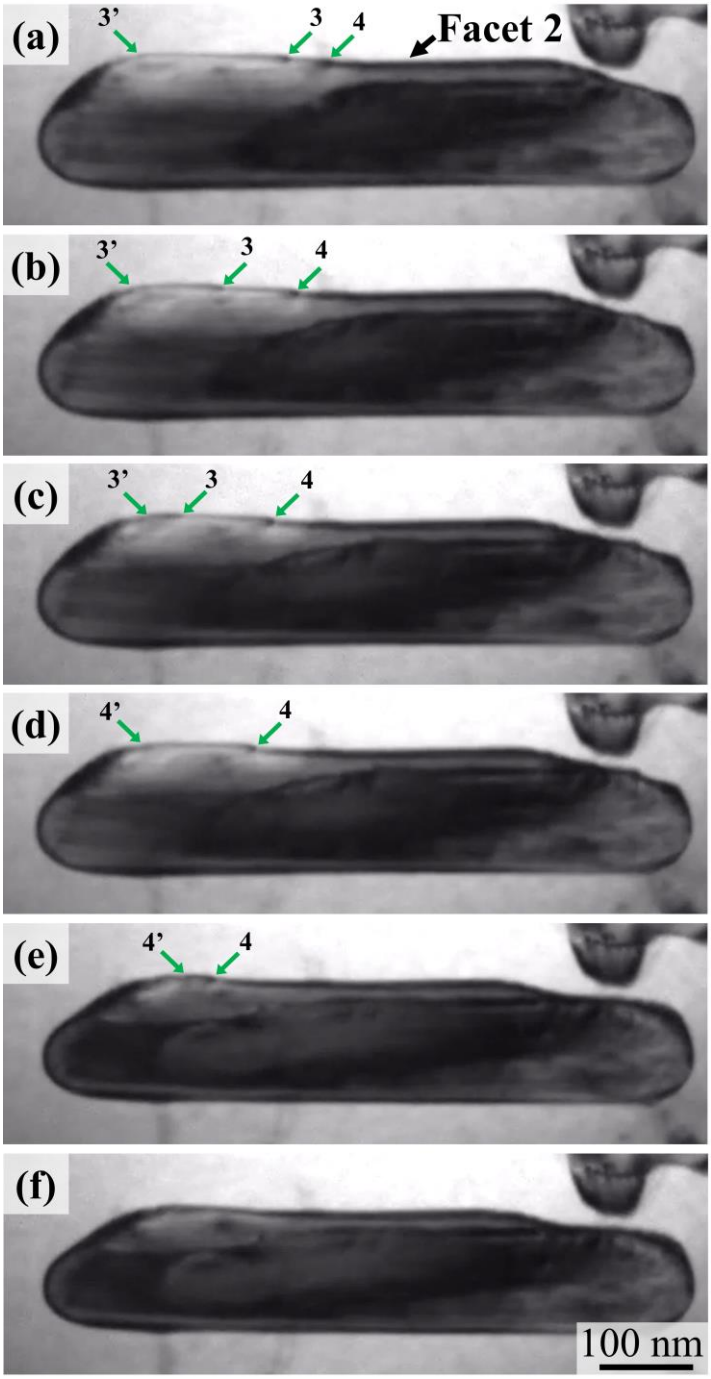

Fig. 13. Annihilation of growth ledges 3 and 4 on Facet 2 at the opposite side of end faces of a β precipitate. Snapshots are taken at (a) 76 s, (b) 80 s, (c) 84 s, (d) 85 s, (e) 98 s, and (f) 99 s in the Supplementary Movie.

The β precipitates with similar morphology and located in a similar area were

characterized post-mortem to elucidate the structures of Facets 1 and 2 since they are likely to have the same variant of the same OR. A precipitate, exhibiting a full Facet 1 and a partially visible end face within the TEM foil, was identified in Fig. 14, where Facet 2 was observed to be highly inclined. The Facet 1 orientation was determined based on the projection-width method [42] as $(\overline{1.37}\ 1.14\ 1.0)_{\beta} \| (\overline{3.6}\ 4.6\ \overline{1.0}\ \overline{0.4})_{\alpha'}$, akin to the habit plane orientation observed in the longer tempered microstructure ($(\overline{1.41}\ 1.01\ 1.0)_{\beta} \| (\overline{4.0}\ 5.0\ \overline{1.0}\ \overline{0.29})_{\alpha'}$). Moreover, the long axis of this precipitate, identified as $[1.6\ 1.0\ 1.1]_{\beta} \| [2.1\ 1.0\ \overline{3.1}\ 0.10]_{\alpha'}$ is also consistent with the previous analysis ($[1.8\ 1.0\ 1.2]_{\beta} \| [2.7\ 1.0\ \overline{3.7}\ 0.16]_{\alpha'}$). The dislocation spacing on the Facet 1, approximately 10 nm, aligns with findings in Fig. 4(b) and previously reported dislocation spacings in α precipitates [8, 11, 24]. Therefore, Facets 1 and 2 in Fig. 11 to Fig**. 13** are probably the habit plane and side facet of the β precipitate, respectively.

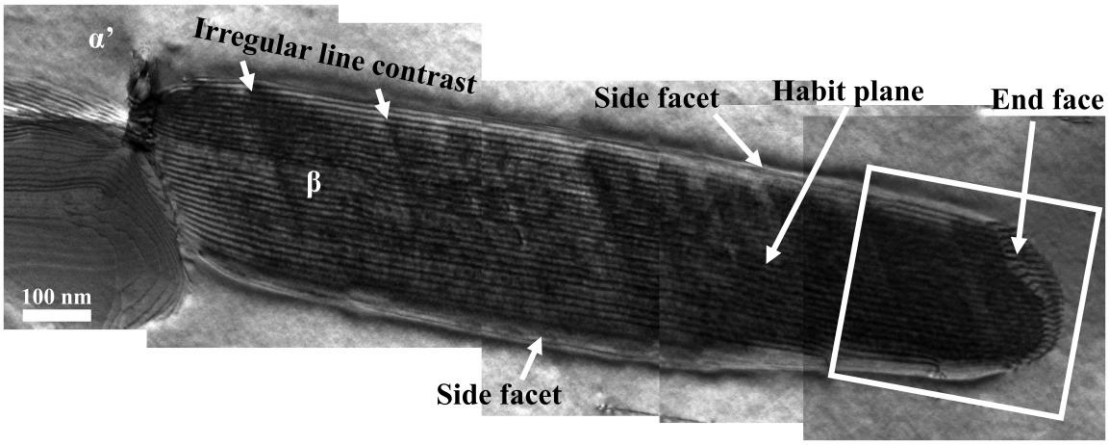

Fig. 14. Bright field image of a β precipitate after in-situ study.

Besides the periodic dislocation lines on the habit plane, irregular linear contrasts are observed on Facet 1 in Fig. 14. Such irregular linear features were often observed in

different precipitation systems, such as α precipitates in Ti alloys [2, 24] and Zr alloys [44], and Cr-rich precipitates in Cu [45] and Ni [46-49]. Those irregular linear features are likely growth ledges that are associated with dislocations. While it is difficult to define the height of growth ledges in Fig. 14, a rough estimation can be made for the height of growth ledges on the side facet. They are around several nanometers, as seen from the ledge marked by "4" in Fig. 13(d). These growth ledges are similar to the growth ledges of 10 nm in height observed from the side facet of α precipitate by Furuhara et al. [13, 24].

4. Theoretical calculation and MD simulations

4.1 Interface structures of habit planes

In contrast to a single set of dislocations previously reported on the habit plane of α precipitated from β matrix [8, 11], our observations reveal that the habit plane of β precipitated from supersaturated α matrix, i.e., tempered martensite, often contains two sets of parallel dislocation lines. The Burgers vectors of these dislocations, $\mathbf{b}_1$ and $\mathbf{b}_4$ (Table 2), are the same types of corresponding vectors. If either one became the Burgers vector of a single set of dislocations in a habit plane, the habit plane of the β precipitate would be the same as the habit plane of the α precipitate. Namely, different Burgers vectors correspond to different variants of the same OR.

To examine the variation of the OR and habit plane with the dislocation structures, we conducted a series of revised O-line calculations, in which the habit plane contains an invariant line and misfit displacement is parallel to a selected Burgers vector or a

combination of Burgers vectors. The lattice parameters from experiments (Section 2.3) were adopted in the calculation. The misfit displacement in the habit plane aligns in the direction defined by one of the following vectors, i.e., $\mathbf{b}_1$, $-\mathbf{b}_4$, $\mathbf{b}_1 - \mathbf{b}_4$, and $2\mathbf{b}_1 - \mathbf{b}_4$, which is guided by the observed dislocation ratios as seen in Fig. 4(e). The results are displayed in a $[111]_\beta$ polar figure (**Fig. 15**) with quantitative data in Supplementary Materials.

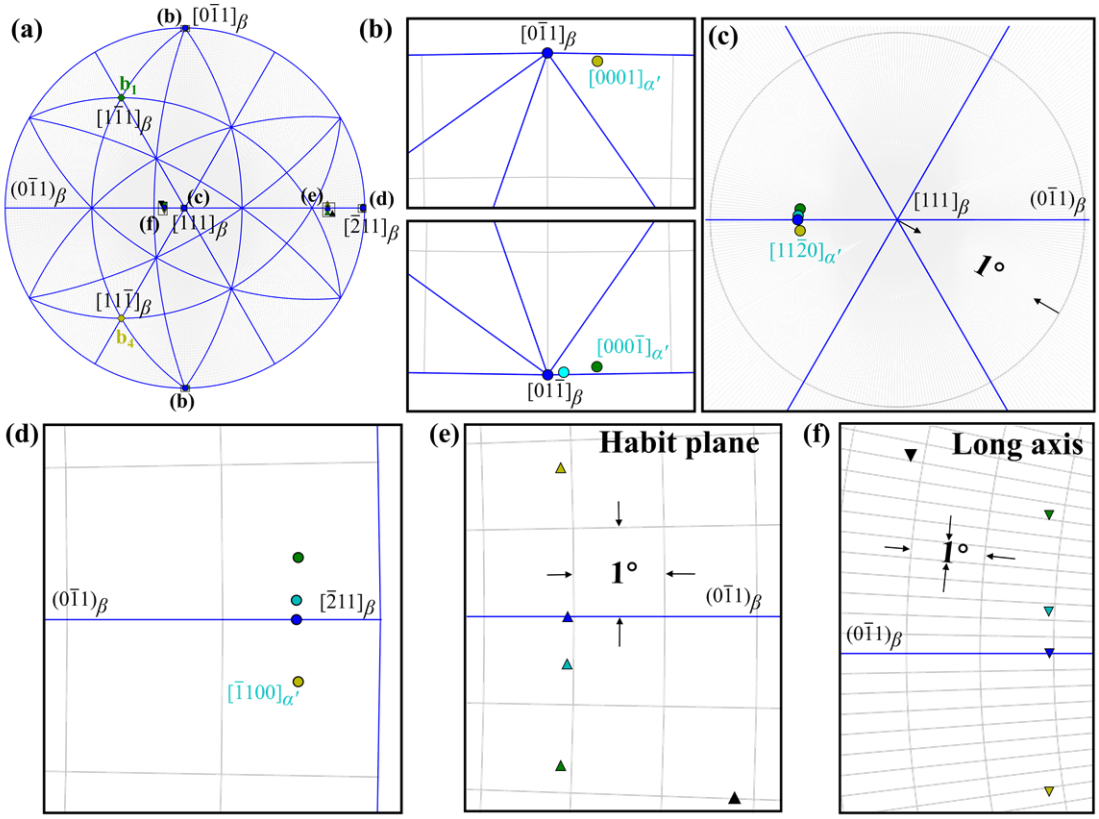

Fig. 15. Crystallographic features predicted by the O-line model using different misfit displacements, plotted in a $[111]_\beta$ polar figure. (b)-(f) are enlarged figures of boxed areas in (a). O-line solutions of $\mathbf{b}_1$, $\mathbf{b}_4$, $\mathbf{b}_1-\mathbf{b}_4$, and $2\mathbf{b}_1-\mathbf{b}_4$ are represented by green, yellow, blue, and cyan. Circles in (b)-(d) represent calculated $[0001]_\alpha$, $[11\bar{2}0]_\alpha$, and $[\bar{1}100]_\alpha$ orientations. (e) and (f) show habit plane normals and long axis directions,

respectively, with black triangles as the average directions from experiments.

All the ORs solved corresponding to the habit planes containing one or two sets of parallel dislocation in **Fig. 15** deviate slightly from the ideal Burgers OR. The specific deviation is required for all misfit displacements in the habit plane to align in one direction defined by the selected Burgers vector(s). It is likely the Burgers OR originates during the nucleation stage and the early growth stage, in which the preferred interface probably starts as an atomically flat plane parallel to the good matching plane $(\bar{1}100)_\alpha \| (\bar{2}11)_\beta$. In this interface, the misfit displacement field is in two dimensions, with the misfit δ = 1.4% (referred to α) along $[0001]_\alpha \| [0\bar{1}1]_\beta$ and δ = 4.3% along $[11\bar{2}0]_\alpha \| [111]_\beta$. The evolution of the habit plane deviating from $(\bar{1}100)_\alpha \| (\bar{2}11)_\beta$ may be understood with two types of rotations, though these two types are not separable in real cases. The first type is due to the formation of interfacial steps. The habit plane tends to contain atomic steps, also called structural ledges [13] or disconnections [8], so that the misfit displacement in a direction near $[11\bar{2}0]_\alpha \| [111]_\beta$ in the terrace plane defined by $(\bar{1}100)_\alpha$ and $(\bar{2}11)_\beta$ can be accommodated by the misfit displacement associated with the step, as demonstrated in a 2D invariant line model [50]. Such a 2D invariant line probably evolves from the ideal Burgers OR, as shown approximately as the trace of the habit plane in Fig. 3(b). If the Burgers OR remains unchanged, the misfit between the step heights defined in different lattices will accumulate. The long-range effect of this slight misfit can be eliminated via a minor rotation (Type I) between $(\bar{1}100)_\alpha$ and $(\bar{2}11)_\beta$ [51, 52]. Consequently, the overall misfit along a direction

crossing steps becomes zero, and this direction defines an invariant line in the habit plane. It is possible to keep $[0001]_\alpha$ and $[0\bar{1}1]_\beta$ parallel as the rotation axis for such a rotation.

Though a β precipitate growing along the invariant line does not require any dislocations, dislocations are needed to eliminate the long-range misfit strain in the interfaces as the β precipitate grows along other directions. It is a property of an invariant line strain that the misfit displacement vectors associated with any point in the interface containing an invariant line must lie all in one direction [53]. When parallel $[0001]_\alpha$ and $[0\bar{1}1]_\beta$ directions lie in the habit plane containing an invariant line, misfit displacement between $[0001]_\alpha$ and $[0\bar{1}1]_\beta$ defines the misfit displacement of any vector in the habit plane. Therefore, the Burgers vector of the dislocations in the habit plane must be $[0001]_\alpha$ or $[0\bar{1}1]_\beta$ defined in different lattices, which is $\mathbf{b}_1 - \mathbf{b}_4$. The O-line solutions of the OR, habit plane, and the long axis corresponding to this Burgers vector are displayed in **Fig. 15**. However, this Burgers vector does not agree with the observation of mixed dislocations with the Burgers vectors of $\mathbf{b}_1$ and $\mathbf{b}_4$. One cannot rule out the possibility of nucleation of <**c**> dislocations (Burgers vector of $[0001]_\alpha$) from the matrix, followed by its decomposition into a pair of dislocations with smaller Burgers vectors of $\mathbf{b}_1$ and $\mathbf{b}_4$ to reduce the total energy of the dislocations [54]. Note that each dislocation with either $\mathbf{b}_1$ or $-\mathbf{b}_4$, is associated with either inserting or missing one layer of terrace plane $(\bar{2}11)_\beta$. This will lead to a rotation with the rotation axis parallel to the dislocations, which is almost perpendicular to $[0001]_\alpha$ or $[0\bar{1}1]_\beta$. When the numbers of $\mathbf{b}_1$ and $-\mathbf{b}_4$ dislocations are equal, the average of the misfit

displacement in the habit plane remains parallel to $[0001]_\alpha$ and $[0\bar{1}1]_\beta$, which can be parallel to each other macroscopically.

The rotation in the OR in the second step is due to the non-equal number of $\mathbf{b}_1$ and $-\mathbf{b}_4$. When their numbers are different, as observed, there will be an angular deviation between $[0001]_\alpha$ and $[0\bar{1}1]_\beta$, as well as a rotation (Tyep II) between the terrace planes defined in different lattices. The total rotation in the OR must permit the total misfit in the habit plane to agree with the dislocations of various Burgers vectors, as can be determined with the revised O-line condition. The calculated results agree with the present experimental data for the Burgers vectors using $2\mathbf{b}_1 - \mathbf{b}_4$. Because the ratio of dislocations with Burgers vectors of $\mathbf{b}_1$ and $\mathbf{b}_4$ is not constant, the deviation between $[0001]_\alpha$ and $[0\bar{1}1]_\beta$ may lead to a true scatter in the OR, which may be buried in the uncertainty in the measurement (**Fig. 15** (a)). Based on the revised O-line calculation, the invariant line direction and especially the habit plane normals for the $\mathbf{b}_1$ and $\mathbf{b}_4$ are not far from each other, as seen in **Fig. 15**. This indicates that in this system the coexistence of dislocation structures with different Burgers vectors in one interface and with one OR may not cause a significant elastic distortion. On the other hand, the size of the habit plane in the present study is small (several hundred nanometers) and hence a small long-range strain may be tolerated. As the precipitate grows large, the nucleation of the habit plane may tend to contain either one of the two type dislocations, since they are crystallographically equivalent, as observed in the habit planes of α precipitates which usually have considerably large size [11].

To determine the structure with two sets of dislocations on the habit plane, we

employed the generalized O-element calculation [18]. Fig. 16(a) shows the calculation results using the OR solved at the condition that the misfit displacement in the habit plane is along $2\mathbf{b}_1 - \mathbf{b}_4$. In this figure, the dots represent edge-on generalized O-lines, and the solid lines in different colors mark the positions of O-cell walls associated with different Burgers vectors. The intersections of the habit plane (dashed line) with O-cell walls define the possible locations of dislocations with the Burgers vectors of $\mathbf{b}_1$ and $\mathbf{b}_4$ in a ratio of 2:1 in the interface. The prediction by the geometric model is corroborated by a relaxed bicrystal model using molecular dynamics. In Fig. 16(b), the interface is viewed along the $[11\bar{2}0]_\alpha \| [111]_\beta$ direction, which is close to the invariant line. The dislocations in the interface and their Burgers vectors have been identified using the Nye tensor method (Section 2.2), consistent with the calculation result in Fig. 16(a). The two types of dislocations are also verified with Burgers circuits, as in Fig. 16(c) and (d), which are fully consistent with the HAADF- STEM image in Fig. 4(e). The interface viewed from along $[0001]_\alpha \| [0\bar{1}1]_\beta$ shows a coherent structure, as seen in Fig. 16(e), in agreement with the HAADF-STEM image in Fig. 3(b). This is because the interface trace line is now almost parallel to the invariant line, along which perfect matching can be realized and hence no dislocation is needed.

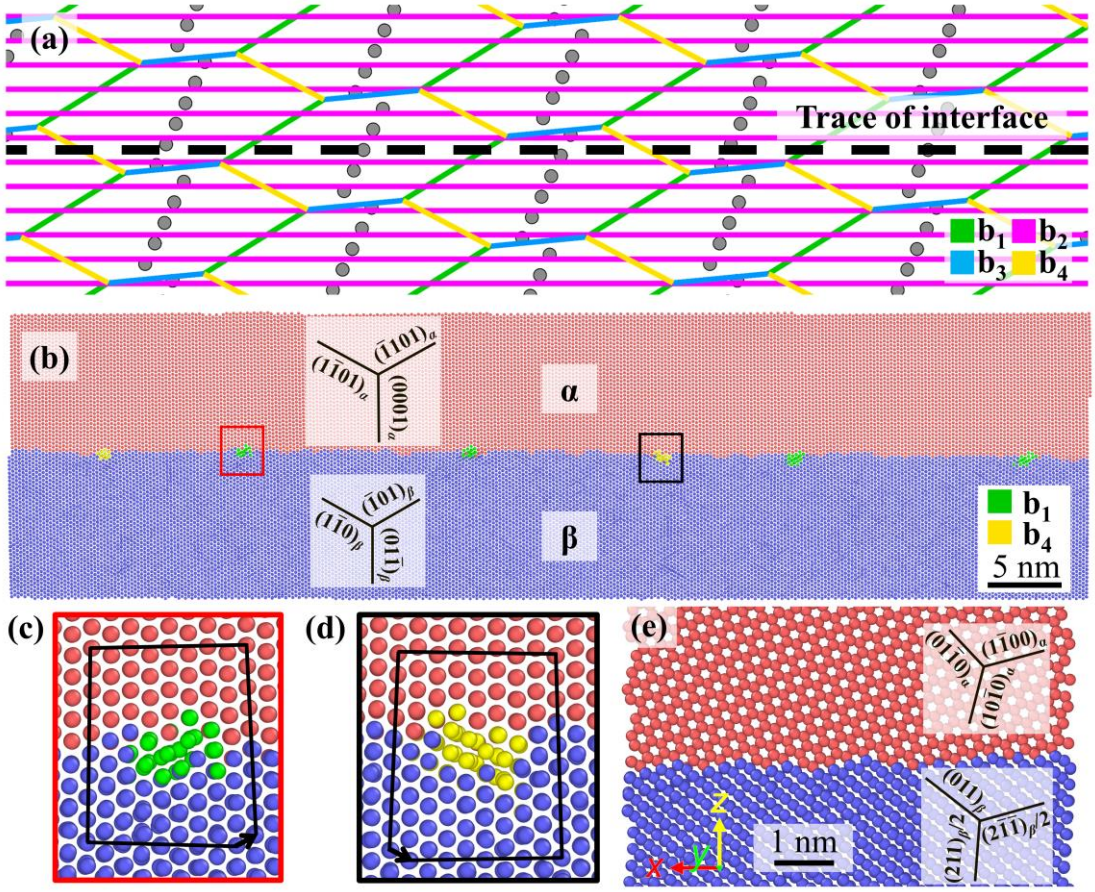

Fig. 16. The α/β habit plane containing two sets of dislocations. (a) Calculation results based on the generalized O-element approach. Dots are the edge-on generalized O-lines and the solid lines are edge-on O-cell walls, viewed along the invariant line direction. The dashed line is the trace of the interface. (b) The atomic images of the interface viewed along $[11\bar{2}0]_\alpha \| [111]_\beta$. The red and blue atoms are in α and β phases, respectively. Green and yellow atoms are near the dislocation cores of $\mathbf{b}_1$ and $\mathbf{b}_4$, respectively. (c) An enlarged image of a $\mathbf{b}_4$ dislocation inside the red rectangle of (b). (d) An enlarged image of a $\mathbf{b}_1$ dislocation inside the black rectangle of (b). (e) The atomic images of the interface viewed along $[0001]_\alpha \| [0\bar{1}1]_\beta$.

It was shown that the interface containing a single set of dislocations is associated

with a local minimum in the interfacial energy [15, 29]. The interfacial energy of the interface in Fig. 16(b) has been calculated and compared with that of the interface containing only one set of dislocations with the Burgers vector of $\mathbf{b}_1$ (with the geometry defined in Fig. 2 and interface structure in the Supplementary Materials). Surprisingly, the calculated interfacial energies for both interfaces have identical values of 0.28 J/m^2. This result explains that the interface with two sets of dislocation is also energetically favorable as observed experimentally. However, the arrangement of $\mathbf{b}_1$ and $\mathbf{b}_4$ dislocations observed in experiments is not strictly periodic as shown in Fig. 16, which may result from random nucleation of either type to accommodate the misfit between $[0002]_\alpha$ and $[0\bar{1}1]_\beta$ in the terrace plane. Such a non-periodic arrangement may cause some fluctuation of local interface geometry (such as OR), while one interface geometry is used for each calculation. From Fig. 15, one can see that the fluctuation caused by different dislocation arrange is very small in this system, thus it is expected to be energetically tolerant.

Another reason for the observation of two sets of dislocations is possibly related to the process of dislocation generation. In contrast to our findings for β precipitates, a transition from coherent to semicoherent interfaces containing one set of dislocations was observed in α precipitates of varying sizes [55]. Such discrepancies suggest that the matrix phase might influence the generation of dislocations on the habit plane. Prior investigations [56, 57] have highlighted the pivotal role of matrix dislocations in the variant nucleation of precipitates, which may also influence the selection of interface dislocations during the coherency loss stage. The primary dislocations existing within

the α matrix are <**a**> type screw dislocations [58-60], which cannot accommodate the misfit between $[0002]_\alpha$ and $[0\bar{1}1]_\beta$ in the habit plane. Instead, they may accommodate misfit on the side facets effectively since $\mathbf{b}_2$ dislocations on the side facet are <**a**> type dislocations of a near screw character. However, the Burgers vector of dislocations on the habit plane, expressed as $<111>_\beta/2$ in β phase, is a common dislocation type in the β matrix. Therefore, a $<111>_\beta/2$ type dislocation available in the β matrix may lead to a preferential dislocation on the habit plane of a nearby α precipitate, resulting in a single set of dislocations on its habit plane. As discussed above, the two sets of dislocations in the habit plane of β precipitates may initiated from the decomposition of <c> dislocations as needed for the misfit strain field in the habit plane. Unfortunately, however, the details of dislocation generation and evolution were not observed in the present study and are unavailable in the literature.

4.2 Interface structures surrounding a 3D precipitate

A geometric configuration of the 3D precipitate is approximated using major interfaces observed experimentally, namely, the habit plane, side facet, and curved end face. In addition to the habit plane, the dislocations structures in a side face and the end face were also calculated using the same OR for the habit plane containing two sets of dislocations as in Fig. 16. According to the previous study, the orientation of the side facet can be calculated by a reciprocal vector of $\Delta\mathbf{g}_{(0\bar{1}1)_\beta}$, defined by $\Delta\mathbf{g}_{(0\bar{1}1)_\beta} = \mathbf{g}_{(0\bar{1}1)_\beta} - \mathbf{g}_{(0002)_\alpha}$ [10]. The calculated interface normal is $(\overline{0.11}\ \overline{0.62}\ 0.78)_\beta \parallel (\overline{0.08}\ 0.10\ \overline{0.02}\ 0.99)_\alpha$, with an angle of 81.5° to the habit plane. A closed trace of habit

planes and side facets is constructed by crossing the edge-on generalized O-lines, as shown in Fig. 17(a). The shape of interface traces is in reasonable agreement well with the edge-on morphology of β precipitate in Fig. 1(d).

By employing the generalized O-element approach in the 3D space, the dislocation structure of the 3D precipitate is calculated, as depicted in Fig. 17(b). The habit plane is characterized by parallel dislocation lines of $\mathbf{b}_1$ and $\mathbf{b}_4$, aligning with the results discussed in the preceding section. The side facet is marked by dislocation lines of $\mathbf{b}_2$ with a fine spacing (1.6 nm) and more widely spaced (7.4 nm) dislocation lines of $\mathbf{b}_3$, with the latter consistent with HAADF-STEM images in Fig. 6. The absence of dislocations with $\mathbf{b}_2$ in these images is understandable. This is because the beam direction is parallel to $\mathbf{b}_2$ so that $\mathbf{b}_2$ does not have any component to yield a close failure of Burgers circuit associated with the dislocations. The dislocation structures on the end face are defined by a coarse-spaced network of $\mathbf{b}_1$, $\mathbf{b}_3$, and $\mathbf{b}_4$ dislocation segments and fine-spaced $\mathbf{b}_2$ dislocation lines. As can be seen from Fig. 17, the fine-spaced $\mathbf{b}_2$ dislocations in the end face continue from the side face. The existence of this set of dislocations is confirmed in Fig. 8(d), observed in the end face. The calculated dislocation structure is further validated through molecular dynamics simulations. The shape of the interfaces in Fig. 17(b) is taken to construct an atomic bicrystal model. Given the low efficiency of the deep neural network potential, the model predominantly includes the region proximal to the end face, including the entire end face and marginal segments of adjacent habit planes and side facets. This atomic model, comprising approximately 2.7 million atoms, undergoes relaxation via molecular dynamics and

energy minimization as outlined in Section 2.2. The relaxed dislocation structures, showcased in Fig. 17(c) with atoms in the α matrix removed, demonstrate remarkable concordance between theoretical predictions and simulations. This study, in contrast with previous theoretical analyses of 3D α precipitates satisfying O-line conditions [6, 15], elucidates the applicability of our theoretical framework to more intricate scenarios involving 3D precipitates devoid of single periodic dislocation sets on the habit plane.

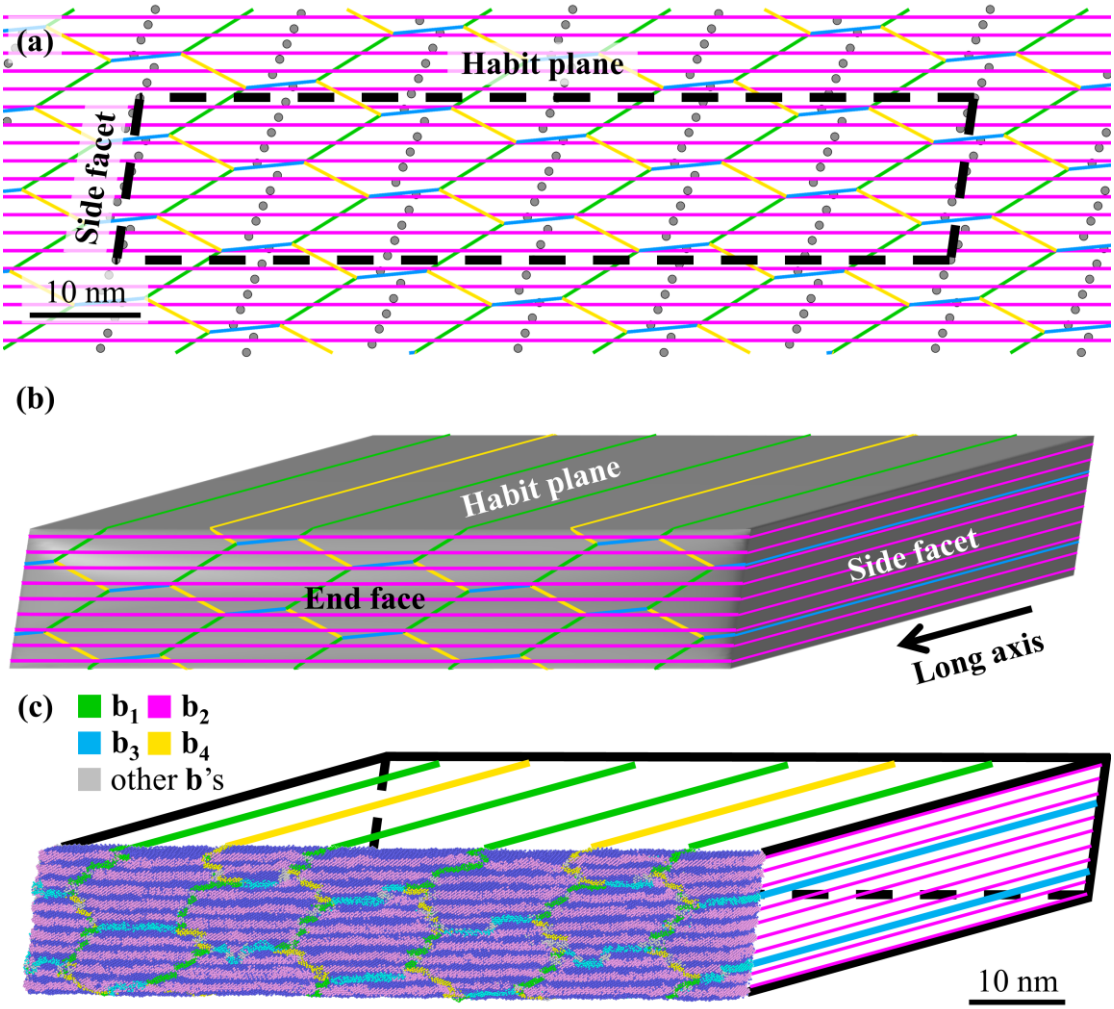

Fig. 17. Dislocation structures on the interfaces around a 3D precipitate with the habit plane containing $\mathbf{b}_1$ and $\mathbf{b}_4$ dislocation lines. (a) Calculation results based on the generalized O-element approach. Dots are the edge-on generalized O-lines and the solid

lines are edge-on O-cell walls, viewed along the invariant line direction. The dashed lines are the traces of habit planes and side facets. (b) The calculated 3D dislocation structure by the generalized O-element approach, with distinct Burgers vectors represented by varying colors for clarity. The viewing direction is slightly tilted from the long axis. (c) Relaxed dislocation structure in the vicinity of the end face. Blue atoms are β phase and the dislocation cores with different Burgers vectors are shown by other colors. The remaining regions of the precipitate are delineated by line sketches.

The atomic model of the interfacial structure in Fig. 17(c) can be sliced into foils with different normals to compare with high-resolution HAADF-STEM images. While the atomic structures of the habit plane are shown in Fig. 16, the illustrations below focus on the side facet and end face. Fig. 18 shows the atomic structures of two near edge-on interface portions viewed in two orientations, so that the fine-spaced dislocations are near edge-on orientations in an end face and a side facet respectively (Fig. 18(a)). The interface in Fig. 18(b) is viewed from $[111]_\beta | [11\bar{2}0]_\alpha$, so the habit plane and side face are approximately edge-on. In this figure, $\mathbf{b}_3$ dislocations on the side facet with a projected spacing of 7.2 nm can be identified by the Burgers circuit. However, $\mathbf{b}_2$ dislocations are not identified by the Burgers circuit. The result of the Burgers circuits in Fig. 18(b) is consistent with that derived from HAADF-STEM images in Fig. 7. The interface in Fig. 18(c) is viewed along $[0\bar{1}1]_\beta | [0001]_\alpha$, so the habit plane and end face are approximately edge-on. The cores of $\mathbf{b}_1$, $\mathbf{b}_2$, $\mathbf{b}_3$, and $\mathbf{b}_4$ dislocations are also identified by the Burgers circuits in Fig. 18(c). It is difficult to

identify the coexistence of multiple sets of dense dislocations with high-resolution TEM, though two closely located dislocations ($\mathbf{b}_2$ and either $\mathbf{b}_1$ or $\mathbf{b}_4$) have been identified experimentally in Fig. 8(c). In contrast to Fig. 18(c), the dislocation lines in Fig. 8 do not appear edge-on due to the curvature of the end face, making them difficult to investigate in the low-index beam direction. The Burgers vectors and the locations of the dislocations in Fig. 18 are characterized by the Nye tensor analysis based on 3D atom positions, which demonstrates the advantage of the atomic model in overcoming the limitation of the experimental results.

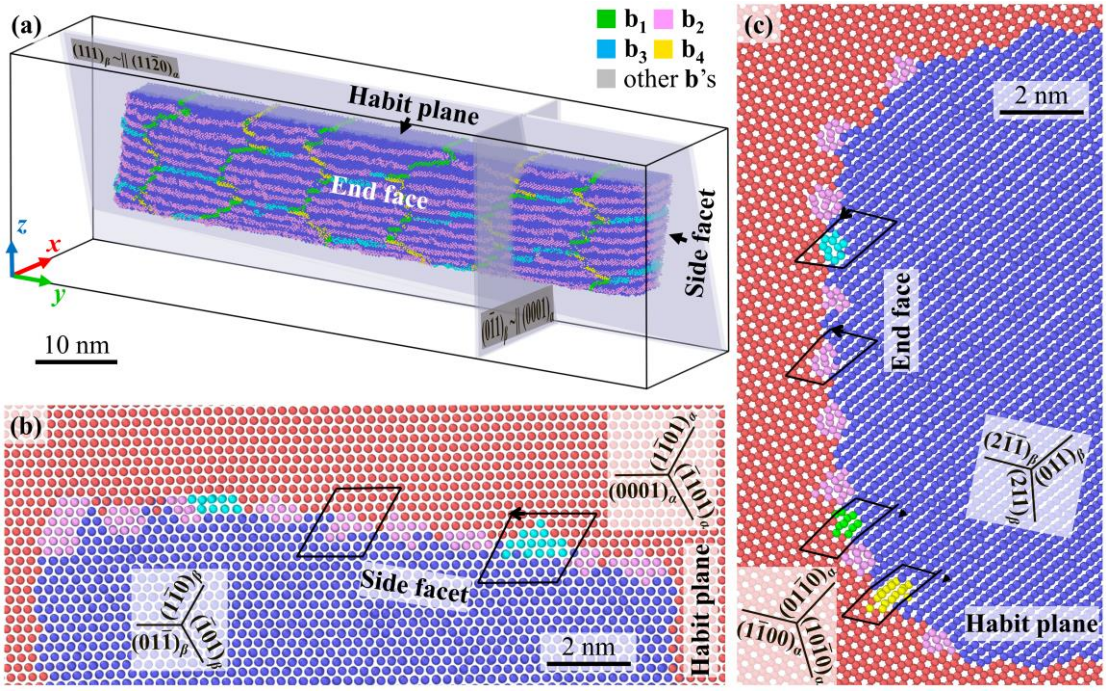

Fig. 18. Atomic image of side facet and end face surrounding the simulated 3D β precipitate. (a) The positions and orientations of cutting planes with respect to the simulated β precipitate. Atoms in the α matrix are removed. (b) Atomic image viewed along $[11\bar{2}0]_\alpha \| [111]_\beta$. (c) Atomic image viewed along $[0001]_\alpha \| [0\bar{1}1]_\beta$. Blue and red atoms are identified as β and α phases, respectively. Atoms of other colors are near the

dislocation cores of different Burgers vectors.

4.3 Possible structures and migration modes of growth ledges

The role of the growth ledges brings the motion of terraces, as suggested in the ledge mechanism in various books [61, 62], is confirmed in the present in-situ TEM study. The fast motion of both the end face and the ledge riser along the invariant line direction is evident in the present experimental observation. Our result verifies that the faceted interfaces containing the invariant line, both the habit plane and side facet, cannot move continuously in the direction normal to themselves at the present experimental condition. The movement of the positions of these interfaces is assisted by the motion of the growth ledges. Similarly, the ledge riser is unmovable when it contains the invariant line. In the present study, the interface migrates as the β precipitate shrinks. The formation of a ledge loop does not require the generation of new dislocations associated with the ledges. Instead, a ledge often starts near a curved end face and then retreats towards the other end face. The ledge disappears somewhere when it meets a ledge of the same height generated from the other end face.

Characterizing the structures of growth ledges on the facets of β precipitates presents significant challenges from an experimental point of view. However, the application of the generalized O-element approach offers a novel avenue for investigating the potential structures of growth ledges. This methodology has been successfully applied to the semicoherent growth ledge structures of γ precipitates in duplex stainless steels, as illustrated in Fig. 7 of ref. [18]. Due to the quasi-periodic distribution of the

generalized O-lines that represent the positions of minimal misfit, there are discrete preferred positions of the habit plane and side facet. By connecting facets across different layers of generalized O-lines, three distinct types of growth ledges are depicted: Fig. 19 (a) presents an edge-on view along the long axis, while Fig. 19(b) offers an inclined perspective from the long axis. Because the discrete preferred the positions, a certain value approximately exists for a unit height of one type of ledge. That is why the ledges initiated from different ends often annihilate when they meet each other. For the same reason of discrete preferred positions of terrace planes of ledges, risers of growth ledges also tend to stay at certain positions to lower the overall interface energy caused by misfit. The smooth migration of any interface containing the invariant line, the habit plane, the side facet, or a riser towards a direction perpendicular to itself will experience resistance due to the rise of interfacial energy. When the driving force is not sufficiently high, probably in the condition of the present in-situ heating, the displacement of the habit plane and side facet must be assisted by the motion of the growth ledges, and the displacement of the risers must be assisted by the motion of the kinks along them. The ledge and kink structures are confirmed in the present experiments and a previous study [13].

On the habit plane, growth ledge 1 in Fig. 19, is characterized by its minimal height and a riser containing a single $\mathbf{b}_2$ dislocation (noted for its fine spacing on the side facet). It is difficult to ascertain whether the mobile ledges and the irregular defects are this type of ledges. This type of ledge has been identified on the habit plane of β precipitates in a Zr-Nb alloy (refer to Fig. 3 in [63]), with the observed ledge height (1.5 nm)

aligning closely with the present theoretical prediction (1.4 nm) once lattice parameter differences between Zr and Ti are considered. Growth ledges 1 may accumulate into taller ledges, comprising multiple $\mathbf{b}_2$ dislocations, which was observed in ref. [12]. Strain accumulation, resultant from the inability of a single set of $\mathbf{b}_2$ dislocations to accommodate misfit on the riser, may necessitate the introduction of dislocations with Burgers vector of $\mathbf{b}_3$ for further misfit relaxation—akin to the misfit accommodations on the side facet to form growth ledge 2. This type of ledge features multiple $\mathbf{b}_2$ dislocations and a single $\mathbf{b}_3$ dislocation, as shown in Fig. 19. While large growth ledges on α precipitate habit planes have been documented [14], the structure of this specific ledge type warrants further empirical validation through high-resolution TEM.

Growth ledges on the side facet may incorporate $\mathbf{b}_1$ or $\mathbf{b}_4$ dislocations on their risers, mirroring dislocations in the habit plane. An instance of a growth ledge containing a $\mathbf{b}_1$ dislocation, designated as Growth ledge 3 in Fig. 19 with a 12 nm height, shows consistency with prior TEM findings of 10 nm height growth ledges on α precipitate side facets [13, 24], possibly corresponding with migrating ledges in Fig. 12 and Fig. 13.

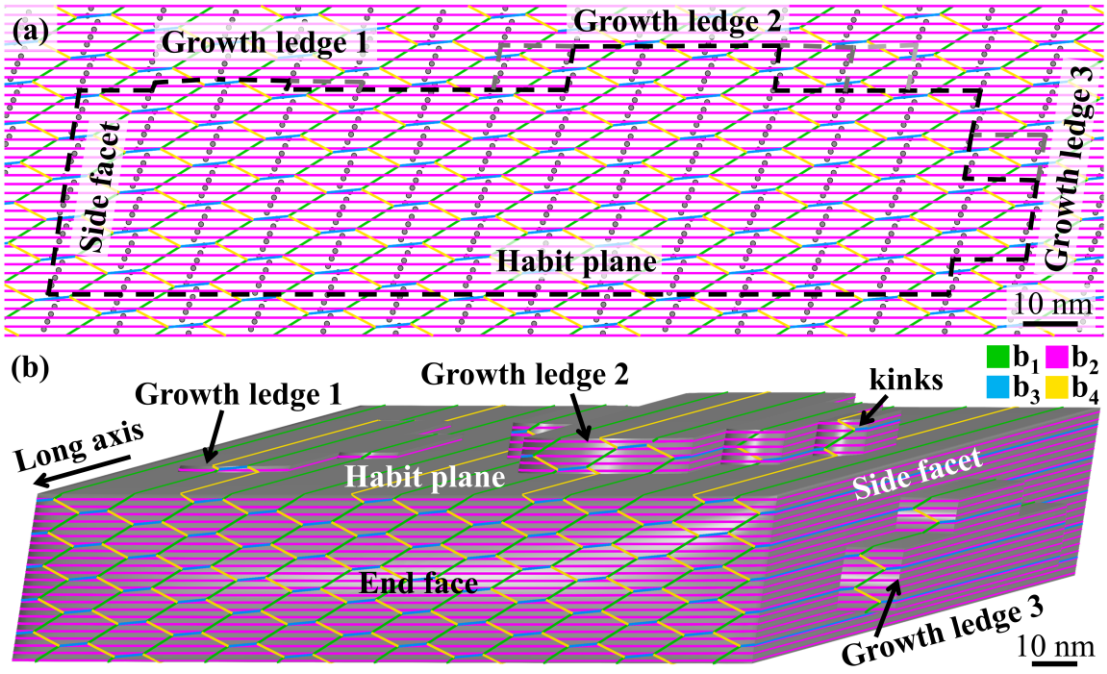

Fig. 19. Possible growth ledge structures on the facets of 3D precipitate based on results of the generalized O-element approach. (a) The traces of interfaces and growth ledges (dashed lines). Dots are the edge-on generalized O-lines and the solid lines are edge-on O-cell walls, viewed along the invariant line direction. (b) The calculated dislocation structures on the interfaces and growth ledges surrounding the 3D precipitate. Burgers vectors of dislocations are represented by varying colors of solid lines for clarity.

Being associated with dislocations, the growth ledges also play a role of accommodating misfit strain at the interface. It is complicated that the motion of these ledges carries the dislocations of multiple types. The migration probably involves a climb motion of the dislocations—a hypothesis proposed by previous research [25], since the terrace planes of the ledges do not serve as slip planes for these dislocations. Further study, through experimental and simulation methodologies, is required to

elucidate the dislocation motion process more comprehensively.

It is realized that the growth ledge mechanism is not the sole mode for interface migrations containing invariant lines. Continuous motion of such an interface is usually associated with a shear deformation [19, 20]. Whether a phase transformation proceeds with a growth ledge mode or a shear-coupled mode depends on the transformation conditions, such as chemical driving force, mechanical constraints, and thermal activations. The ledge mechanism likely works for precipitates transformed in bulk when the driving force is not very large since the shear-coupled mode will experience a large mechanical constraint inserted by its surrounding matrix. The selection of growth mode in a given phase transformation condition remains imperative for future quantitative investigations that integrate the thermal dynamics, kinetics, and crystallography.

5. Conclusions

In this investigation, we carefully examined the structure and migration of three typical portions of the interface surrounding a β precipitate in the α′ matrix in a Ti-2.6 wt% Mo alloy. Utilizing a synergistic approach involving TEM, molecular dynamics, and generalized O-element calculations, we unveiled the intricate dislocation and atomic structures on the habit plane, side facet, and end face surrounding the β precipitate. Contrary to a single set of dislocations typically observed on the habit plane of α precipitates, our study discovers the coexistence of two sets of dislocations on the habit plane of β precipitate, with Burgers vectors $\mathbf{b}_1=[2\bar{1}\bar{1}3]_{\alpha'}/6|[1\bar{1}1]_{\beta}/2$ and $\mathbf{b}_4=$

$[2\bar{1}\bar{1}\bar{3}]_{\alpha'}/6\,|\,[11\bar{1}]_{\beta}/2$. The difference in the habit plane dislocations between β precipitates (two sets) and α precipitates (one set) may result from the available dislocations within the matrix phase. The side facets and end faces of β precipitates display dislocation configurations akin to their α counterparts. Specifically, the side facets contain two sets of parallel dislocations with $\mathbf{b}_2=[11\bar{2}0]_{\alpha'}/3\,|\,[111]_{\beta}/2$ for the fine-spaced set and $\mathbf{b}_3=[2\bar{1}\bar{1}0]_{\alpha'}/3\,|\,[100]_{\beta}$ for the coarse-spaced set, while the end face contains fine-spaced $\mathbf{b}_2$ dislocation lines and coarse-spaced networks consisting of $\mathbf{b}_1$, $\mathbf{b}_3$, and $\mathbf{b}_4$ dislocation segments. A continuous picture of interface structures around a β precipitate was determined by a combinatorial calculation of the generalized O-element approach and molecular dynamics using deep neural network potential. The theoretical results on different portions of the interface agree with the TEM observations from these interface structures.

In-situ TEM studies revealed that the migration of habit plane and side facet in β precipitates proceed via a lateral motion of nano-sized growth ledges. The dislocation structures on the growth ledges are analyzed based on the generalized O-element approach, demonstrating potential non-conservative motion of dislocations while the growth ledge migrates laterally on the facet on the β precipitate. This finding offers a deeper comprehension of the microstructure evolution during phase transformation and lays the groundwork for future atomistic and mesoscale modeling of the precipitation process in titanium alloys.

Acknowledgements

We would like to thank Prof. Xin-Fu Gu at the University of Science and Technology Beijing for his help with the usage of PTCLab. Supports from the National Key Research and Development Program of China (Grant No. 2016YFB0701304) and the National Natural Science Foundation of China (Grant No. 51871131) are gratefully acknowledged. Y. -S. Zhang acknowledges the Chinese Scholarship Council (No. 201906210303) for funding the stay at CEMES in Toulouse, France. J. -Y. Zhang gratefully acknowledges the support from the CNRS/IN2P3 Computing Center (Lyon - France) for providing computing and data-processing resources needed for this work.

References

[1] M. Peters, C. Leyens, Titanium and titanium alloys, Springer-Verlag, Berlin Heidelberg, 2003
[2] D. Banerjee, J.C. Williams, Perspectives on titanium science and technology, Acta Mater. 61(3) (2013) 844-879
[3] G. Lütjering, J.C. Williams, Titanium, Springer-Verlag, Berlin Heidelberg, 2007
[4] S. Banerjee, P. Mukhopadhyay, Phase transformations, examples from titanium and zirconium alloys, Elsevier, Oxford, 2007
[5] W.G. Burgers, On the process of transition of the cubic-body-centered modification into the hexagonal-close-packed modification of zirconium, Phys. 1 (1934) 561-586
[6] Y.-S. Zhang, J.-Y. Zhang, W.-Z. Zhang, Dislocation network on the curved end face of α precipitates in a Ti-8 wt.% Fe alloy, Phil. Mag. 102(5) (2021) 375-388
[7] Y. Zheng, W.A.T. Clark, H.L. Fraser, Characterization of the interfacial structure of coarse α precipitates in a metastable β-Ti alloy Ti-5Al-5Mo-5V-3Cr, JOM 71(7) (2019) 2291-2295
[8] Y.F. Zheng, R.E.A. Williams, G.B. Viswanathan, W.A.T. Clark, H.L. Fraser, Determination of the structure of α-β interfaces in metastable β-Ti alloys, Acta Mater. 150 (2018) 25-39
[9] Y.M. Zhu, S.M. Zhu, M.S. Dargusch, J.F. Nie, HAADF-STEM study of phase separation and the subsequent α phase precipitation in a β-Ti alloy, Scr. Mat. 112 (2016) 46-49
[10] F. Ye, W.-Z. Zhang, Dislocation structure of non-habit plane of α precipitates in a Ti–7.26 wt.% Cr alloy, Acta Mater. 54(4) (2006) 871-879
[11] F. Ye, W.-Z. Zhang, D. Qiu, A TEM study of the habit plane structure of

intragrainular proeutectoid alpha precipitates in a Ti-7.26 wt%Cr alloy, Acta Mater. 52(8) (2004) 2449-2460
[12] M.J. Mills, D.H. Hou, S. Suri, G.B. Viswanathan, Orientation relationship and structure of α/β interfaces in conventional titanium alloys, Boundaries & Interfaces in Materials: the David A. Smith Symposium, Indianapolis, Indiana, U.S., 1998, pp. 295-301
[13] T. Furuhara, T. Ogawa, T. Maki, Atomic-structure of interphase boundary of an α-precipitate plate in a β Ti-Cr alloy, Phil. Mag. Lett. 72(3) (1995) 175-183
[14] E.S.K. Menon, H.I. Aaronson, Interfacial structure of Widmanstatten plates in a Ti–Cr alloy, Acta Metall. 34(10) (1986) 1975-1981
[15] J.-Y. Zhang, F.-Z. Dai, Z.-P. Sun, W.-Z. Zhang, Structures and energetics of semicoherent interfaces of precipitates in hcp/bcc systems: A molecular dynamics study, J. Mater. Sci. Technol. 67 (2021) 50-60
[16] S. Wang, T. Wen, J. Han, D.J. Srolovitz, Coherent and semicoherent α/β interfaces in titanium: structure, thermodynamics, migration, npj Comput. Mater. 9(1) (2023) 216
[17] A. Rida, S.I. Rao, J.A. El-Awady, Interaction of ⟨*a*⟩ prismatic screw dislocations with the *α*–*β* interface side face in *α*–*β* Ti alloys, Acta Mater. 260 (2023) 119337
[18] J.-Y. Zhang, Y. Gao, Y. Wang, W.-Z. Zhang, A generalized O-element approach for analyzing interface structures, Acta Mater. 165 (2019) 508-519
[19] J.-Y. Zhang, Z.-P. Sun, D. Qiu, F.-Z. Dai, Y.-S. Zhang, D. Xu, W.-Z. Zhang, Dislocation-mediated migration of the α/β interfaces in titanium, Acta Mater. 261 (2023) 119364
[20] D. Qiu, M.-X. Zhang, P.M. Kelly, T. Furuhara, Crystallography of surface precipitates associated with shape change in a Ti–5.26 wt.% Cr alloy, Acta Mater. 61(20) (2013) 7624-7638
[21] C.J. Rosa, Oxygen diffusion in alpha and beta titanium in the temperature range of 932° to 1142°C, Metall. Trans. 1(9) (1970) 2517-2522
[22] X. Fu, X.-D. Wang, B. Zhao, Q. Zhang, S. Sun, J.-J. Wang, W. Zhang, L. Gu, Y. Zhang, W.-Z. Zhang, W. Wen, Z. Zhang, L.-q. Chen, Q. Yu, E. Ma, Atomic-scale observation of non-classical nucleation-mediated phase transformation in a titanium alloy, Nat. Mater. 21(3) (2022) 290-296
[23] H.M. Flower, S.D. Henry, D.R.F. West, The β ⇄ α transformation in dilute Ti-Mo alloys, J. Mater. Sci. 9(1) (1974) 57-64
[24] T. Furuhara, J.M. Howe, H.I. Aaronson, Interphase boundary structures of intragranular proeutectoid α plates in a hypoeutectoid Ti-Cr alloy, Acta Metall. Mater. 39(11) (1991) 2873-2886
[25] W. Bollmann, Crystal lattices, interfaces, matrices, Bollmann W, Geneva, 1982
[26] W. Bollmann, Crystal defects and crystalline interfaces, Springer-Verlag, Berlin, Heidelberg, 1970
[27] W.-Z. Zhang, G.R. Purdy, O-lattice analyses of interfacial misfit. II. Systems containing invariant lines, Phil. Mag. A 68(2) (1993) 291-303
[28] X.-F. Gu, T. Furuhara, W.-Z. Zhang, PTCLab: free and open-source software for calculating phase transformation crystallography, J. Appl. Cryst. 49(3) (2016) 1099-

1106
[29] F.-Z. Dai, W.-Z. Zhang, A simple method for constructing a reliable initial atomic configuration of a general interface for energy calculation, Model. Simul. Mater. Sci. Eng. 22(3) (2014) 035005
[30] J. Guénolé, W.G. Nöhring, A. Vaid, F. Houllé, Z. Xie, A. Prakash, E. Bitzek, Assessment and optimization of the fast inertial relaxation engine (FIRE) for energy minimization in atomistic simulations and its implementation in lammps, Comput. Mater. Sci. 175 (2020) 109584
[31] E. Bitzek, P. Koskinen, F. Gähler, M. Moseler, P. Gumbsch, Structural relaxation made simple, Phys. Rev. Lett. 97(17) (2006) 170201
[32] L. Zhang, J. Han, H. Wang, W. Saidi, R. Car, W. E, End-to-end symmetry preserving inter-atomic potential energy model for finite and extended systems, Proceedings of the 32nd International Conference on Neural Information Processing Systems, NIPS'18, Curran Associates, Inc., 2018, pp. 4441-4451
[33] L. Zhang, J. Han, H. Wang, R. Car, W. E, Deep potential molecular dynamics: A scalable model with the accuracy of quantum mechanics, Phys. Rev. Lett. 120(14) (2018) 143001
[34] A.P. Thompson, H.M. Aktulga, R. Berger, D.S. Bolintineanu, W.M. Brown, P.S. Crozier, P.J. in 't Veld, A. Kohlmeyer, S.G. Moore, T.D. Nguyen, R. Shan, M.J. Stevens, J. Tranchida, C. Trott, S.J. Plimpton, LAMMPS - a flexible simulation tool for particle-based materials modeling at the atomic, meso, and continuum scales, Comput. Phys. Commun. 271 (2022) 108171
[35] S. Plimpton, Fast parallel algorithms for short-range molecular-dynamics, J. Comput. Phys. 117(1) (1995) 1-19
[36] J. Zeng, D. Zhang, D. Lu, P. Mo, Z. Li, Y. Chen, M. Rynik, L.a. Huang, Z. Li, S. Shi, Y. Wang, H. Ye, P. Tuo, J. Yang, Y. Ding, Y. Li, D. Tisi, Q. Zeng, H. Bao, Y. Xia, J. Huang, K. Muraoka, Y. Wang, J. Chang, F. Yuan, S.L. Bore, C. Cai, Y. Lin, B. Wang, J. Xu, J.-X. Zhu, C. Luo, Y. Zhang, R.E.A. Goodall, W. Liang, A.K. Singh, S. Yao, J. Zhang, R. Wentzcovitch, J. Han, J. Liu, W. Jia, D.M. York, W. E, R. Car, L. Zhang, H. Wang, DeePMD-kit v2: A software package for deep potential models, J. Chem. Phys. 159(5) (2023)
[37] H. Wang, L. Zhang, J. Han, W. E, DeePMD-kit: A deep learning package for many-body potential energy representation and molecular dynamics, Comput. Phys. Commun. 228 (2018) 178-184
[38] P.M. Larsen, S. Schmidt, J. Schiøtz, Robust structural identification via polyhedral template matching, Model. Simul. Mater. Sci. Eng. 24(5) (2016) 055007
[39] A. Stukowski, Visualization and analysis of atomistic simulation data with OVITO-the Open Visualization Tool, Model. Simul. Mater. Sci. Eng. 18(1) (2010) 015012
[40] F.-Z. Dai, W.-Z. Zhang, An automatic and simple method for specifying dislocation features in atomistic simulations, Comput. Phys. Commun. 188 (2015) 103-109
[41] J.F. Nye, Some geometrical relations in dislocated crystals, Acta Metall. 1(2) (1953) 153-162

[42] R.-X. Xie, W.-Z. Zhang, τompas: a free and integrated tool for online crystallographic analysis in transmission electron microscopy, J. Appl. Cryst. 53(2) (2020) 561-568
[43] H. Okamoto, O-Ti (oxygen-titanium), J. Phase Equilib. Diffus. 32(5) (2011) 473-474
[44] W.-Z. Zhang, G.R. Purdy, A TEM study of the crystallography and interphase boundary structure of α precipitates in a Zr-2.5wt%Nb alloy, Acta Metall. Mater. 41(2) (1993) 543-551
[45] M.G. Hall, H.I. Aaronson, K.R. Kinsma, The structure of nearly coherent fcc: bcc boundaries in a Cu-Cr alloy, Surf. Sci. 31 (1972) 257-274
[46] G. Chen, G. Spanos, R.A. Masumura, W.T. Reynolds, Effects of ledge density on the morphology and growth kinetics of precipitates in a Ni-Cr Alloy, Acta Mater. 53(4) (2005) 895-906
[47] J.K. Chen, G. Chen, W.T. Reynolds, Interfacial structure and growth mechanisms of lath-shaped precipitates in Ni-45 wt% Cr, Phil. Mag. A 78(2) (1998) 405-422
[48] T. Furuhara, K. Wada, T. Maki, Atomic-structure of interphase boundary enclosing BCC precipitate formed in FCC matrix in a Ni-Cr alloy, Metall. Mater. Trans. A 26(8) (1995) 1971-1978
[49] T. Furuhara, T. Maki, The role of matrix dislocations in growth ledge formation on f.c.c.-b.c.c. interfaces in a Ni-Cr alloy, Phil. Mag. Lett. 69(1) (1994) 31-36
[50] U. Dahmen, Surface relief and the mechanism of a phase transformation, Scr. Metall. 21(8) (1987) 1029-1034
[51] U. Dahmen, Orientation relationships in precipitation systems, Acta Metall. 30(1) (1982) 63-73
[52] J. Wu, W.-Z. Zhang, X.-F. Gu, A two-dimensional analytical approach for phase transformations involving an invariant line strain, Acta Mater. 57(3) (2009) 635-645
[53] J.S. Bowles, J.K. Mackenzie, The crystallography of martensite transformations I, Acta Metall. 2(1) (1954) 129-137
[54] J.P. Hirth, J. Lothe, Theory of dislocations, 2nd ed., Wiley, New York, 1982
[55] Y. Zheng, R.E.A. Williams, G.B. Viswanathan, W.A.T. Clark, H.L. Eraser, Investigation of α/β interface structure in titanium alloy using HRSTEM, Proceedings of the 13th World Conference on Titanium, John Wiley & Sons, Inc., 2016, pp. 419-423
[56] Y. Zhu, K. Zhang, Z. Meng, K. Zhang, P. Hodgson, N. Birbilis, M. Weyland, H.L. Fraser, S.C.V. Lim, H. Peng, R. Yang, H. Wang, A. Huang, Ultrastrong nanotwinned titanium alloys through additive manufacturing, Nat. Mater. 21(11) (2022) 1258-1262
[57] D. Qiu, R. Shi, D. Zhang, W. Lu, Y. Wang, Variant selection by dislocations during α precipitation in α/β titanium alloys, Acta Mater. 88 (2015) 218-231
[58] T. Tsuru, M. Itakura, M. Yamaguchi, C. Watanabe, H. Miura, Dislocation core structure and motion in pure titanium and titanium alloys: A first-principles study, Comput. Mater. Sci. 203 (2022) 111081
[59] D. Caillard, M. Gaumé, F. Onimus, Glide and cross-slip of **a**-dislocations in Zr and Ti, Acta Mater. 155 (2018) 23-34
[60] A. Rida, S.I. Rao, J.A. El-Awady, Characteristics of ⟨*a*⟩ screw dislocations and

their slip on prismatic and pyramidal planes in pure α titanium from atomistic simulations, Materialia 24 (2022) 101503
[61] D. Porter, K. Easterling, Phase transformations in metals and alloys, Chapman and Hall, New York, 1992
[62] H.I. Aaronson, M. Enomoto, J.K. Lee, Mechanisms of diffusional phase transformations in metals and alloys, CRC Press, Boca Raton, 2010
[63] W.-Z. Zhang, V. Perovic, A. Perovic, G.C. Weatherly, G.R. Purdy, The structure of HCP-BCC interfaces in a Zr-Nb alloy, Acta Mater. 46(10) (1998) 3443-3453